Electronic Theses and Dissertations, 2004-2019

2012

Radiation Effects on Wide Band Gap Semiconductor Transport Properties

Casey Minna Schwarz
University of Central Florida

University of
Central Florida

STARS
Showcase of Text, Archives, Research & Scholarship

RADIATION EFFECTS ON WIDE BAND GAP SEMICONDUCTOR TRANSPORT PROPERTIES

by

CASEY MINNA SCHWARZ
M.S. University of Central Florida, 2009
B.S. University of Central Florida, 2006

A dissertation submitted in partial fulfillment of the requirements
for the degree of Doctor of Philosophy
in the Department of Physics
in the College of Sciences
at the University of Central Florida
Orlando, Florida

Spring Term
2012

Major Professors: Leonid Chernyak
Elena Flitsiyan

ABSTRACT

In this research, the transport properties of ZnO were studied through the use of electron and neutron beam irradiation. Acceptor states are known to form deep in the bandgap of doped ZnO material. By subjecting doped ZnO materials to electron and neutron beams we are able to probe, identify and modify transport characteristics relating to these deep accepter states.

The impact of irradiation and temperature on minority carrier diffusion length and lifetime were monitored through the use of the Electron Beam Induced Current (EBIC) method and Cathodoluminescence (CL) spectroscopy. The minority carrier diffusion length, L, was shown to increase as it was subjected to increasing temperature as well as continuous electron irradiation. The near-band-edge (NBE) intensity in CL measurements was found to decay as a function of temperature and electron irradiation due to an increase in carrier lifetime. Electron injection through application of a forward bias also resulted in a similar increase of minority carrier diffusion length.

Thermal and electron irradiation dependences were used to determine activation energies for the irradiation induced effects. This helps to further our understanding of the electron injection mechanism as well as to identify possible defects responsible for the observed effects. Thermal activation energies likely represent carrier delocalization energy and are related to the increase of diffusion length due to the reduction in recombination efficiency. The effect of electron irradiation on the minority carrier diffusion length and lifetime can be attributed to the trapping of non-equilibrium

electrons on neutral acceptor levels. The effect of neutron irradiation on CL intensity can be attributed to an increase in shallow donor concentration. Thermal activation energies resulting from an increase in L or decay of CL intensity monitored through EBIC and CL measurements for p-type Sb doped ZnO were found to be the range of E_a = 112 to 145 meV.

P-type Sb doped ZnO nanowires under the influence of temperature and electron injection either through continuous beam impacting or through forward bias, displayed an increase in L and corresponding decay of CL intensity when observed by EBIC or CL measurements. These measurements led to activation energies for the effect ranging from E_a = 217 to 233 meV. These values indicate the possible involvement of a Sb_{Zn}-$2V_{Zn}$ acceptor complex.

For N-type unintentionally doped ZnO, CL measurements under the influence of temperature and electron irradiation by continuous beam impacting led to a decrease in CL intensity which resulted in an electron irradiation activation energy of approximately E_a = 259 meV. This value came close to the defect energy level of the zinc interstitial.

CL measurements of neutron irradiated ZnO nanostructures revealed that intensity is redistributed in favor of the NBE transition indicating an increase of shallow donor concentration. With annealing contributing to the improvement of crystallinity, a decrease can be seen in the CL intensity due to the increase in majority carrier lifetime. Low energy emission seen from CL spectra can be due to oxygen vacancies and as an indicator of radiation defects.

This work is dedicated to my family for being as impressed and proud of me now as the day I was born.

ACKNOWLEDGMENTS

It has been a long time since my first entrance into the physics world. When I began I was unsure of how far I could actually go in the field. So, here, I would like to give all my thanks and dedicate this work to the people who knew all along that I would make it all the way.

With my mother's endless encouragement to pursue my degree as well as any extracurricular activities that made me happy along the way, I never thought of giving up. Thank you for always being there, for all the long trips to visit me (helping me move countless times) and for being so easy to talk to and for providing the comfort that no matter what happens I could always go home.

To my father, who with his steady influx of motivation and inspiring quotes (no matter where they actually might have come from), taught me most importantly to enjoy the time I have with the people I love and to not worry so much. He also inspired my love of physics through our love of science fiction.

To my sister, Jenna, who taught me the art of competition and made me a better person by never letting me stop playing.

To all my friends who provided the sometimes necessary distractions of which my life would be uninspired and empty without.

To my dog, Oscar, who waited patiently at my feet all of the long nights studying.

To my future husband, Patrick, who made huge sacrifices I'm not sure I would have the strength to do, just to be by my side while I finished my degree. He makes my apartment a home and calms my heart. The Cooper family also makes a wonderful addition to my family and have readily accepted me into their home with support and encouragement in my work.

To my grandmother who always remained a prominent figure in throughout my life and provided the encouragement I needed to achieve.

To my grandfather who also inspired me to continue in science through his own achievements.

TABLE OF CONTENTS

LIST OF FIGURES

LIST OF TABLES

LIST OF ABBREVIATIONS

A   Amp

Al   Aluminium

Ar   Argon

Au   Gold

B   Boron

C   Carbon

CL   Cathodoluminescence

EBIC   Electron Beam Induced Current

eV   Electron Volt

FCC   Face-Centered Cubic

FET   Field Effect Transistor

GaN   Gallium Nitride

H   Hydrogen

HEMT High Electron Mobility Transistor

Hg   Mercury

In   Indium

K   Kelvin

k_B Boltzmann's Constant

LED   Light Emitting Diode

L_n Minority Carrier Diffusion Length

MBE   Molecular Beam Epitaxy

MOCVD Metal Organic Chemical Vapor Deposition

N   Nitrogen

SEM   Scanning Electron Microscope

Si   Silicon

UV   Ultraviolet

ZnO   Zinc Oxide

μ_p Hole Minority

τ_n Minority Carrier Lifetime

PHYSICAL CONSTANTS

b   Barn $10^{-28} m^2$

k_B Boltzmann's Constant 8.616×10^{-5} eV/K

e   Electron Charge 1.60218×10^{-19} C

eV   Electron Volt 1.6×10^{-19} Joules

CHAPTER ONE – INTRODUCTION

1.1 Background

Wide band gap semiconductors continue to display major advantages in regards to high temperature, high power applications of optoelectronic and photonic devices. Zinc oxide (ZnO) and gallium nitride (GaN) materials have been explored for use as blue and UV optoelectric devices such as detectors and emitters and high temperature electronics [1].

ZnO, due to recent developments in doping and growth, has an increased potential for application. Being a direct wide band gap semiconductor (Eg = 3.35 eV) with high exciton binding energy (60 meV, compared to 25 meV in GaN) makes ZnO an attractive source for minority-carrier based bipolar devices such as light emitting diodes (LEDs) , laser diodes and transparent p-n junctions. ZnO also shows advantages over III-nitride materials due to its lower material cost and availability of large area lattice-matched substrates [2-5]. ZnO has also been shown to have superior resistance to radiation damage than other semiconductor materials. This, in combination with ZnO's excellent optical and electrical properties, could lead to ZnO devices being utilized for space applications [6]. The recent opportunity for ZnO material to be manufactured in the shape of nanowires produces greater prospects for ZnO in the field of solid-state electronics. The large surface area of nanowires in combination with the bio-safe

characteristics of ZnO also makes them attractive candidates for gas, chemical sensing and biomedical applications [7].

Transport properties of minority carriers in ZnO and GaN are of crucial importance for bipolar device function. Functional hetero-junction devices have been produced with ZnO and GaN-based materials; however, crystallographic defects at the interface impede optical and electrical properties, making these structures inferior to homogeneous devices [8-10]. The realization of such ZnO devices is complicated by lack of available quality, highly conductive materials of both n- and p-type. Achieving n-type conductivity in ZnO does not present a problem as even nominally undoped material is generally n-type. This is due to the electrical activity of native defects, such as interstitials, antisites, and oxygen vacancies, as well as hydrogen impurities. Achieving good p-type conductivity has been a major hurdle for developing ZnO p-n junctions due to the high ionization energies of its potential acceptors. This is in addition to the problem of high concentrations of native and unintentional donors, which act as compensating centers and reduce the concentration of free carriers [1].

Recent advances in p-type doping using larger radii atoms, such as antimony (Sb), have produced ZnO homojunctions with good electrical and optical properties [11-12]. However, the performance of bipolar devices can still be limited by the transport properties of minority carriers, even with the production of viable p-type materials. In direct band gap semiconductors, minority carrier diffusion length is usually several

orders of magnitude lower than in indirect band gap materials such as silicon or germanium [1].

Research into the minority carrier diffusion lengths and lifetimes in both n- and p-type ZnO is important due to its direct implication on the performance of bipolar devices. Investigation into the temperature dependence of minority carrier properties is integral when considering applications of these devices in high-temperature electronics [13]. Based on previous studies of thermal and electron injection induced minority carrier diffusion length, L, increase in GaN and limited studies into ZnO it is of interest to examine these properties further in ZnO materials [14-17].

This chapter begins with a crystal structural summary of the properties of ZnO and GaN. This is followed by an overview of acceptor levels in ZnO and GaN. The role of minority carrier diffusion length in bipolar device performance is then discussed and is concluded with the dissertation focus and outline.

1.2 Structural Overview of ZnO and GaN

Zinc oxide (ZnO) is a II-VI compound semiconductor. It is a wide-gap semiconductor containing a direct gap around 3.4 eV in the near UV. Naturally occurring ZnO is referred to as "zincite" and usually consist of a certain amount of Mn and other elements and is a yellow/red color. Synthetic ZnO is used for experimental investigations and, due to its large bandgap, is colorless and clear. Zinc oxide crystallizes mostly in two forms, hexagonal wurtzite and cubic zincblende [18].

Gallium nitride (GaN) is a binary III-V semiconductor with a direct bandgap of 3.4 eV. Like ZnO, GaN can crystallize in the hexagonal wurtzite and cubic zinc blende structure [19]. The common wurtzite structure is shown in Figure 1 and is more stable at ambient conditions than the zinc blende. The wurtzite structure is more energetically favored than the zinc blende for both GaN and AlN [1,18,19].
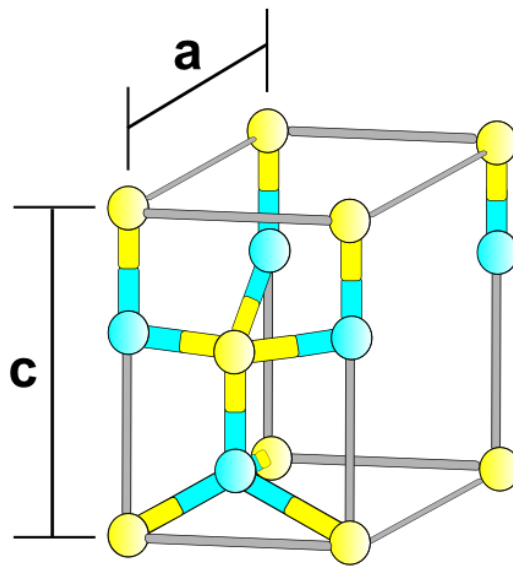
Figure 1. The Wurtzite crystal structure, where c is the height and a is the base of the primitive cell. The yellow spheres correspond to zinc and the blue correspond to oxygen.

The zinc (gallium) and oxide (nitride) centers are tetrahedral; this is the most characteristic geometry for both ZnO and GaN. Both the hexagonal and zinc blende polymorphs do not have inversion symmetry which results in piezoelectricity. The lattice constants for ZnO are a = 3.25 A and c = 5.2 A. The ratio c/a has a value of around 1.60 which deviates slightly from the ideal hexagonal cell value c/a = 8/3 = 1.633. The

wurzite structure has lattice constants for GaN of a = 3.189 A and c = 5.186 A, and a/c = 1.62 which deviates slightly from the ideal hexagonal cell value c/a = 8/3 = 1.633 [1,18].

The cubic zinc blende-type structure can be mostly stabilized by epitaxial growth on cubic substrates. This structure forms a face-centered cubic lattice (fcc). The tetrahedrally coordinated diamond, zinc blende, and wurtzite-type crystal structures are characteristic for covalent chemical binding with sp3 hydrization. ZnO has a substantial ionic bonding component, due to this fraction of ionic binding, the bottom of the conduction band is formed from the 4s levels of Zn^{2+} and the top of the valence band from the 2p levels of O^{2-}. At low temperature, the gap between the conduction band and the highest valence band is approximately 3.437 eV [1,18]. For GaN, at room temperature, the bandgap is around 3.39 eV [19].

1.3 Acceptor levels in ZnO and GaN

It has been theorized by Limpijumnong *et al.* that the role of acceptors in size-mismatched Sb-impurity doped ZnO can be produced by a Sb_{Zn}-$2V_{Zn}$ complex, which is predicted to have an ionization energy of 160 meV [20]. The ionization energy is several times lower than that of a substitutional configuration. Despite the large size mismatch, which in principle should inhibit the substitution of these impurities on the oxygen site, effective p-type doping with hole concentrations up to 10^{20} cm^{-3} can be achieved using Sb [11].

In the past, codoping was suggested as a possible means for obtaining p-type ZnO by enhancing nitrogen solubility in ZnO lowering its ionization energy [21]. However, now we can see that the level of the nitrogen atom on the oxygen site, N_o, is relatively deep. This makes acceptor ionization difficult, and N-doped ZnO could be unstable [22]. Other group-V dopants have been used in the pursuit of p-type ZnO. Several research groups have reported acquiring successful p-type conductivity in ZnO with large-size mismatched dopants such as P [13,23,24], As [25,26] and Sb [27] (atomic radius = 1.06, 1.20, and 1.40 A vs 0.73 A for O). This goes against what was previously thought about dopant size. Also, recent first-principles total energy calculations show that P_o, As_o, or Sb_o all have very high acceptor-ionization energies [20].

In the paper by Limpijumnong a theory is presented for large-size mismatched impurities by first-principles calculations. Isolated Sb may form donor (Sb_{Zn}), deep acceptor (Sb_o) or amphoteric interstitial (Sb_i), but none of these could end in p-typeness, so Sb related defect complexes are considered [20].

Using strain relief and Coulomb interaction it was found that the complex Sb_{Zn}-$2V_{Zn,}$ represents a new class of low energy defects containing shallow acceptor levels. For this complex, the core Sb occupies the Zn antisite, which is the energy needed to spontaneously induce two Zn vacancies. The resulting complex is an acceptor with both low formation energy ($\Delta H_f (0) = 2.00$ eV) and low ionization energy ($\varepsilon(0/-) = 0.16$ eV).

These results show that the suppression of formation of Sb_o by oxygen-rich growth/annealing processes is necessary for successful p-type doping [20].

The Sb_{Zn}-2V_{Zn} model gives insight into puzzling experimental observations in Sb doped ZnO. This proposed model could be useful for more than just p-type ZnO. One could maximize the formation energies of the compensating native defects, such as V_o and Zn_i, while minimizing the dopant by chemical potentials. This goes against currently used doping schemes where the formation energies of the compensating defects are often minimized along with that of the dopant. In codoping, a mechanism where Coulomb binding compensates the cost of creating extra defects in the complex doesn't currently meet expectations. The proposed model by Limpijumnong gives a mechanism through which complexes could become more important than their parent defects [20].

Magnesium (Mg) is the most commonly used dopant for GaN. Mg can act as an acceptor or as a donor. In p-type GaN, the ionization energy levels may range from 140 meV to 210 meV [28] and are not easily ionized at room temperature. Due to this fact, concentration levels of Mg have to be very high in order to produce good p-type material. For $Al_xGa_{1-x}N$ the Mg level will deepen and the bandgap energy will increase as Al is added to GaN [29].

There are other dopants currently being studied and used for GaN, such as carbon (C) and iron (Fe). It has been theorized that carbon, when substituted onto a nitrogen site, can form an acceptor level with ionization energy similar to magnesium [30,31]. Carbon can form both donor and acceptor states in GaN and its concentrations

and stability are strongly affected by growth processes. Some reports achieve p-type conductivity [32,33] while some obtain n-type conductivity [34,35].

Fe and Mn doping in GaN can form acceptor levels, however these form deep levels and [36] hinder the use of Fe and Mn for p-type conductivity. Fe and Mn-doped GaN display ferromagnetic properties at room temperature [37].

1.4 Minority Carrier Diffusion Length function in Bipolar Device Performance

Diffusion is due to the existence of a spatial variation of the carrier concentration inside a semiconductor. The diffusion process is driven by concentration gradients, the carriers will move from areas of high concentration to low concentration, this is known as the diffusion current.   External excitation has a much larger impact on the concentration of minority carrier than on majority ones because generation density is usually much lower than the majority carrier density; it is the minority carriers that are more susceptible to diffusion. The electron diffusion current density is proportional to the gradient of the electron density, *n*, by the following relation [38,39];

$$J_n = eD_n\frac{dn}{dx} \tag{1.1}$$

Where e is the charge of the electron and D_n is the electron diffusion coefficient.

When non-equilibrium carriers are generated in a material due to an external excitation in the absence of an electric field, they will diffuse over a certain distance, in a particular direction, before recombining. The average distance that the carrier has gone

before succumbing to recombination is defined by *L*, the diffusion length, which can be related to carrier lifetime ,*τ*, by the following relation [38,39];

$$L = \sqrt{D\tau} \tag{1.2}$$

Carrier lifetime refers to the time between generation and recombination of non-equilibrium carriers. The Einstein relationship connects the mobility μ and the diffusion current D_n by [38,39];

$$D_n = \frac{kT}{e}\mu \tag{1.3}$$

Where k is the boltzmann's constant and T is the temperature.

When in the vicinity of a p-n junction (Schottky barrier), non-equilibrium minority carrier generated by an external excitation within a few diffusion lengths of the space charge region can be collected by the built in electric field and add to the current flow across the device. The amount of current collected depends on the diffusion length of the carriers and thus relates to the overall efficiency of the device [38.39].

1.5 Dissertation Focus and Outline

In order to promote the greater and more versatile use of ZnO materials in the device world we need to develop a clear understanding of its transport properties critical for its use in bipolar devices. We know we are limited by the lack of available stable p-type conductivity as well as the inherently short diffusion length of minority carriers. In

regards to space applications it is also important to have knowledge of ZnO radiation hardness.

It will be shown that by use of the electron injection either through continuous electron beam impacting or forward biasing we can significantly increase the minority carrier diffusion length in Sb doped ZnO materials. Temperature dependent measurements showed that the activation energies associated with this electron injection process were indicative of a Sb_{Zn}-$2V_{Zn}$ acceptor complex. Cathodoluminescence experiments led to a corresponding decrease in intensity with temperature and electron injection which yielded similar activation energies further supporting the indication of a Sb_{Zn}-$2V_{Zn}$ acceptor complex as a perpetrator of these effects [40-42].

The effects of neutron irradiation on ZnO material will be studied. The effect of dose on carrier lifetime will be shown through a decrease in CL intensity indicative of an increase in carrier lifetime. This is associated with an increase of shallow donor concentration [43,44].

1.5.1 Dissertation Layout

Chapter two will introduce the experimental process of techniques used during this study, including EBIC and CL methods. First, sample growth techniques and preparation will be shown. Then, theoretical models for determining minority carrier lifetime and diffusion length will be derived and illustrated. The work space as a whole

will be shown and the importance of each individual piece will be displayed. Next, the Electron Beam Induced Current Method (EBIC) will be discussed and its set up will be shown as well as the experimental determination of diffusion length and thermal activation energy. Then, the Cathodolumenscence (CL) method will be discussed and its set up shown as well as how to determine experimental thermal activation energy. Electron beam and forward bias electron injection will be discussed as well as the methods of determination of their activation energies.

Chapter three places each individual experiment into separate sections for clarity. In this chapter, a detailed description of each sample used, the technique used to examine it and the results will be presented. The main topics are temperature and irradiation effects of ZnO through analysis of minority carrier transport properties.

Chapter four will contain the theoretical discussions of the outcomes of this dissertation.

Chapter five concludes the major findings of this research.

In appendix section A, related experiments to the previous research is shown. Experiments concerning the minority carrier diffusion length and lifetime through thermal activation energies is seen in p-type neutron irradiated ZnO nanowires and is discussed. Also, thermal activation energies of AlGaN/GaN HEMT devices subjected to degradation testing is shown. Diffusion length measurements of InAIN/GaN devices after the effects of proton irradiation dose are shown.

CHAPTER TWO – EXPERIMENTAL PROCESS AND TECHNIQUES

This section includes information on all of the experimental methods and techniques utilized in the experiments contributing to this study. Molecular Beam Epitaxy (MBE), Metal Organic Chemical Vapor Deposition (MOCVD) and Plasma Assisted Molecular Beam Epiatxy (PAMBE) were the main methods for sample growth and preparation. Details into these techniques will be first discussed. Growth methods used for individual samples will be addressed in Section 3.

To investigate the effects of irradiation, two major experimental techniques were used to probe the samples. These techniques included Electron beam induced current (EBIC) and Cathodoluminescence (CL). The EBIC technique gave information on how the injection of electrons affected the electrical properties of the sample. CL measurements gave an understanding of the optoelectric properties of the sample as well as changes in carrier lifetime related to irradiation effects. Equipment set up and operation for both procedures and techniques will be shown including specific parameters used for the experiments. The contribution to the overall analysis of the sample will then be discussed.

2.1 Sample Growth and Characterization

Molecular beam epitaxy (MBE) is a method which allows for epitaxial growth through the interaction of one or several molecular or atomic beams on a surface of a

heated crystalline substrate. The slow deposition rate is key to epitaxially grown films. This technique makes use of an ultra-high vacuum (10^{-8} Pa). Solid sources materials are put in evaporation cells in order for an angular distribution of atoms or molecules in a beam to be provided. The substrate is then heated to the necessary temperature and may be rotated to improve on the homogeneity of the growth [45].

Chemical vapor deposition (CVD) is a growth technique using reactant gases which flow over a substrate and grow films or nanowires. Metal Organic Chemical Vapor Deposition (MOCVD) method is used for nitride or III-V semiconductor deposition. This process is ideal for growing multiple epitaxial layers needed for device structures. The growth of crystals is by chemical reaction and not by physical deposition as in MBE [19].

Plasma Assisted Molecular Beam Epitaxy (PAMBE) uses oxygen plasma generated by a radiofrequency system to improve the MBE ZnO nanowire growth.

2.1.1 The p-n Junction

In order to proceed into experimental set up and measurement it is first important to describe the fundamental properties of a p-n junction. A p-n junction is created when a p-type and an n-type semiconductor are in contact. This p-n junction is a bipolar device where both the holes and electrons participate in the conduction process. A p-n junction is a rectifier of current, meaning that it allows current to flow easier in or is bias in one direction. When the p and n-type regions are made from the same material, it is said that the junction is a homo-junction. If the semiconductor material is different then

is it referred to as a hetero-junction. Many devices utilize p-n junctions including bipolar transistors [39].

We now look into an unbiased p-n junction at thermodynamic equilibrium. When first bringing together the p-type and n-type sides of the junction electron diffuse from the n-type region into the p-type region and the holes from the p-type region go into the n-type region. Due to the charge displacement, an internal built-in potential is formed at the junction. When the electrons diffuse from the n-type region to the p-type region they leave behind ionized donor atoms. These atoms cannot move within the crystal and occupy substitutional sites in the crystal lattice. This creates the depletion region. Now there is a positive charge in the depletion region which attracts the electrons and pushes then into the p-type region. This force is balanced by the force of the built-in electric field pushing the electrons back to the n-type side. Likewise, the diffusion of holes from the p-type into the n-type region leads to a depletion or space-charge region in the p-type material as shown in Figure 2. When the junction is at thermal equilibrium, the drift current from the electric field and the diffusion current from the concentration gradient equal each other. To have this thermal equilibrium calls for the Fermi levels, E_f, to be equal and constant. The Fermi level is the maximum energy of an electron in the material at zero degree Kelvin. Also, the Fermi level is an energy level that has a 50% probability of being filled with electrons, even within the band gap. A built in potential, V, in the p-n junction is created when the Fermi levels for both the n and p type materials exist at the same level [38,39].
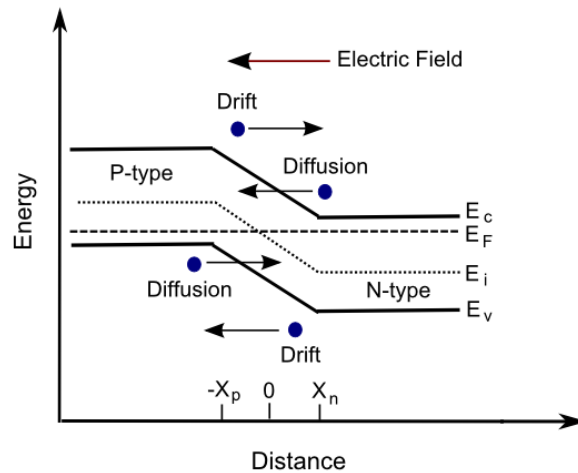
Figure 2. Energy band diagram of a p-n junction. Depletion region is located from $-X_p$ to X_n. Illustrated here are the drift and diffusion currents of the electrons and holes.

2.1.2 Forward Bias

An external bias, V_a, is applied to the junction and considered positive if the potential of the p-type region is larger than that of the n-type region. To apply this forward bias you need to connect the p-type side to a positive terminal while the n-type side is connected to a negative terminal. As a forward bias is being applied to a p-n junction it makes the energy levels in the p region lower than in the n region and decreases the electric field in the space-charge region. This decrease opens the gate for an increase in flow of electrons from the n to p region and an increase of holes from the p to n region [39].

The holes from the p-type region and the electrons from the n-type region are pushed together towards the junction and reduce the width of the depletion zone. Applied to the p-type material, the positive charge repels the holes and on the n-type material the negative charge repels the electrons. As electrons and holes are pushed

15

towards the junction, the distance between them decreases, thus lowering the potential barrier.

The electric field eventually won't be able to counteract the charge carrier motion across the p-n junction and the electrical resistance is subsequently reduced. The electrons crossing the p-n junction into the p-type region, or holes to the n-type, will diffuse into the near neutral zone. The amount of minority carrier diffusion in the near neutral regions determines the amount of current that may flow through the diode.

The majority carriers, electrons in n-type or holes in p-type, can flow through a semiconductor for a macroscopic length. A forward bias causes a force that pushes the electrons across the junction from the n to the p side. Since the depletion region is small enough, electrons can cross the junction and inject into the p-type material. They cannot simply continue to flow indefinitely due to recombination with holes being energetically favorable to them. Before recombining the electrons will flow for an average length in the p-type material (usually a number of microns), this is called the diffusion length, *L*.

The electric current continues uninterrupted even as electrons only penetrate a short distance into the p-type material because the holes also flow in the opposite direction. Due to Kirchoff's current law, the total current is constant in space. The flow of holes from the p-type region into the n-type region is exactly equal to the flow of electrons from the n to p regions [38.39].

2.1.3 Hall Measurements

In order to identify the carrier concentration and mobility of a sample, measurements were made based on the Hall effect. If a magnetic field is applied perpendicular to the direction of carrier flow in a semiconductor sample, a potential difference emerges in the direction perpendicular to both the current flow and the magnetic field as shown in Figure 3. This is because each electron in motion experiences a Lorentz force proportional to the strength of the field and the velocity at which it is traveling through it and is strongest when its motion is perpendicular to B. The Lorentz force is responsible for the electron accumulation at one edge of the sample and the electric field resulting from the uneven charge distribution. This potential difference is the Hall voltage. Since the current is still able to continue to flow in the material we know that the Lorentz force is balanced by the force on the electrons by the electric field. From these properties, information about the sample may be calculated.
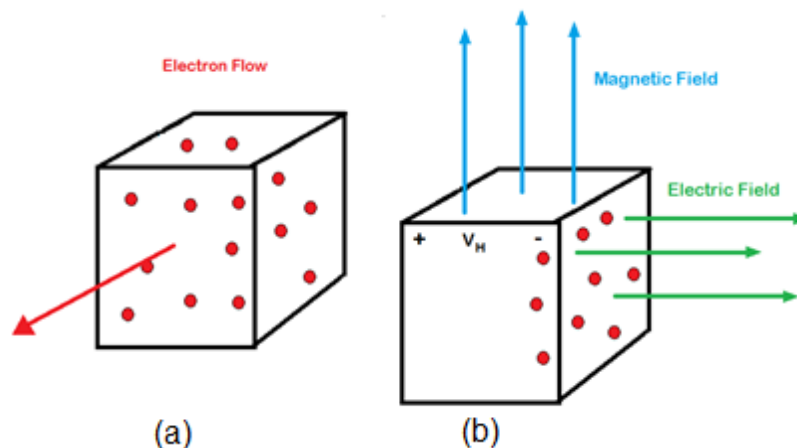
Figure 3. (a) Electrons are flowing opposite the direction of current. (b) A magnetic field induces an electric field perpendicular to it. The electrons collect on the right.

The van der Pauw method is commonly used to extract the resistivity and hall coefficient of a specific sample. The sample must have a thickness much less than its width and length, preferably symmetric and have no isolated holes. Four small ohmic contacts, placed on the boundary of the sample, are used for measurements. From these measurements certain properties of the material such as doping type, sheet carrier density and mobility can also be calculated [38].

2.2 The Experimental Workspace

All experiments were conducted *in-situ* in a Phillips XL30 scanning electron microscope (SEM) with accelerating voltages up to 30kVs. The SEM allows for a high degree of spatial resolution (2-3 nm at 30kV for highly conductive samples). An external Gatan temperature control allows for the acquisition of temperature dependent measurements from -196°C to 200°C. A Gatan MonoCL3 cathodoluminescence system is attached to the SEM allowing for the optical measurements to be performed also *in-situ*. A Hewlett-Packard 4145A semiconductor parameter analyzer allows for the application of a forward bias to the p-n junction of the sample. The workspace as a whole is shown in Figure 4.

Figure 4. This EBIC and CL workstation includes the SRS current preamplifier (1), the Keithley voltmeter (2), SEM (3), Gatan Mono CL3 monochromator (4), Gatan Temperature controller (5) and the 4145A Semiconductor Parameter Analyzer (6).

2. 3 Methods for determining Minority carrier lifetime and Diffusion length

There are two major experimental methods used to investigate the effects of irradiation on semiconductor material. The EBIC technique provided us with information on how the irradiation affected the electrical properties of the sample such as the minority carrier diffusion length while CL measurements gave input on how this affected the optoelectric properties of the sample such as carrier lifetime. EBIC is similar to CL as they both depend on the creation of electron hole pairs by the SEM's electron beam in the semiconductor sample.

2.3.1 Electron Beam Induced Current Method

The Electron Beam Induced Current (EBIC) method is a convenient and popular method for measurements of minority carrier diffusion lengths. The measurements are done *in-situ* in a scanning electron microscope (SEM) with simple sample preparation. In the following experiments, the electron beam of the SEM Philips XL 30 irradiated the samples to produce the Electron Beam Induced Current technique. Accelerating voltages from 20kV to 30kV corresponding to penetration depths of 1.2-2.5 μm were used. Temperatures in the range of 25-125°C were used.

2.3.1.1 EBIC Experimental Setup

The EBIC set up consist of a SRS current preamplifier (1), Keithley voltmeter (2) and the SEM (3) as illustrated in Figure5.
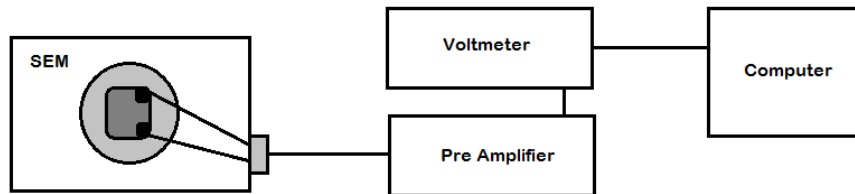
Figure 5. Diagram of the EBIC setup. Inside the SEM the sample is hooked up through two contacts. Then the signal is directed to the Pre Amplifier and digitized using the voltmeter. From there a computer collects and records the data.

From the sample the SRS current preamplifier is used to adjust sensitivities. From there the pre amplifier sends the signal to the Keithley 2000 voltmeter, where it is converted to a digital signal displayed on a computer. The PC displays the voltage versus the distance scanned by the electron beam. A picture of the Phillips XL30 SEM workstation is seen in Figure 6.

Figure 6. This is the Phillips XL30 SEM workstation used during the experiment. This station includes the SEM vacuum and sample chamber (1), electron beam column (2), secondary electron detector (3), Gatan Mono CL3 monochromator (4) and the Hamamatsu photomultiplier tube (5).

The EBIC method uses a Schottky barrier or a p-n junction to collect the current coming from the non-equilibrium minority carriers generated by the beam of the SEM. Figure 7 is a diagram of the perpendicular configuration used to collect EBIC measurements from the p-n junction of the sample. The sample is positioned so that EBIC line scans will go in a direction perpendicular across the p-n junction. As the beam moves away from the barrier/junction in a line scan mode, the current decays as fewer and fewer minority carriers are able to diffuse to the space charge region [46,47]. Most

line scans take between 12 and 24 seconds to complete. When the temperature is being changed the electron beam is turned off and a new area is selected to avoid contamination from the previously selected site.
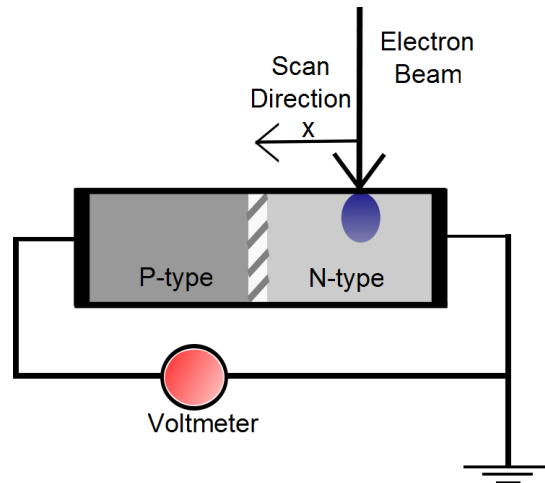
Figure 7. Experimental Setup for the EBIC measurements represented in perpendicular p-n configuration. The space-charge region is denoted with cross hatchings.

2.3.1.2 Determining Diffusion Length and Thermal Activation Energy

The EBIC technique is dependent on the non-equilibrium carriers generated in semiconductors under the influence of electron beam irradiation and their resulting separation by the built in field of the p-n junction or Schottky diode. As majority carriers are swept away from the region of the p-n junction's built-in field localization, the minority ones instead build up and strengthen the magnitude of the overall electric current. When the beam moves further away from the p-n junction in a line scan mode, the current will decay as less minority carriers are able to diffuse to the space charge region. By measuring the EBIC current dependence on the distance from the p-n

22

junction and with the use of Equation 1.3, the minority carrier diffusion length, *L*, can then be extracted from the EBIC line scan [48]. The exponential decay of the EBIC signal versus distance from the p-n junction interface is fitted to Equation 2.1:

$$I = Ad^{\alpha}\exp(-\frac{d}{L})$$ (2.1)

where I is the EBIC signal, A is a constant, d is beam-to-junction distance, and *L* is the diffusion length. The coefficient, α, responsible for surface recombination, v_s, was taken to equal -1/2. For two asymptotic cases, Boersma found that for v_s = 0, α=-1/2 and for v_s = ∞, α=-3/2 [48]. Since the exponential term which dominates the values of I_{EBIC} is independent of α, if the value of α is chosen to be anything between -3/2 and -1/2 the diffusion length is altered by less than 20% [48,49].

Taking the natural logarithm of Equation 2.1 gives us:

$$\ln(Id^{\alpha}) = -\frac{x}{L} + ln(A)$$ (2.2)

An example of an EBIC line scan exponential decay from the p-n junction is shown below in Figure 8.
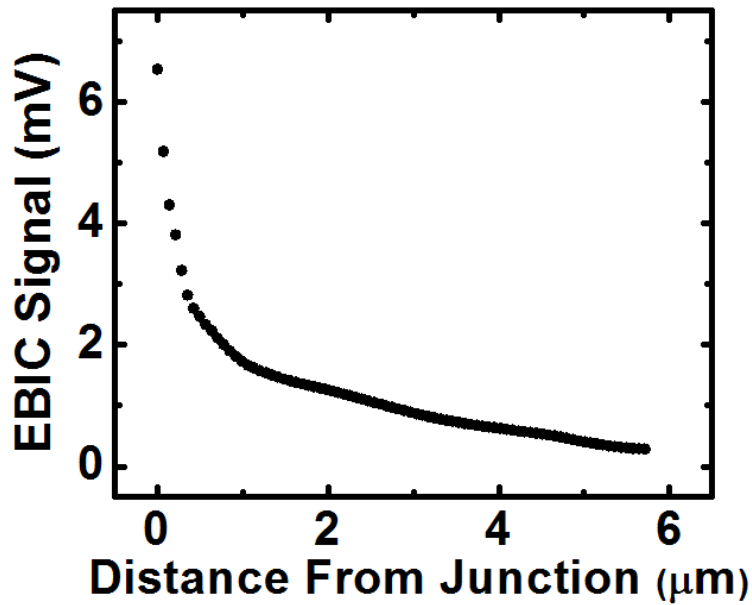
Figure 8. Graph of the EBIC signal (mV) versus the distance from the p-n junction in μm.

Since we have V vs. Distance some manipulation will have to be made to fit into

Equation 2.2. Using the sensitivity from the SRS pre amplifier, we multiply the selected

sensitivity (A/V) by the Voltage acquired in the EBIC scan and get a value for our

Current (I) in the Equation 2.2. Then, when you plot $\ln(Id^\alpha)$ as a function of d, shown in

Figure 9, you should get a linear line which slope yields $-\frac{1}{L}$. This is accurate for as long

as x > 2 L.
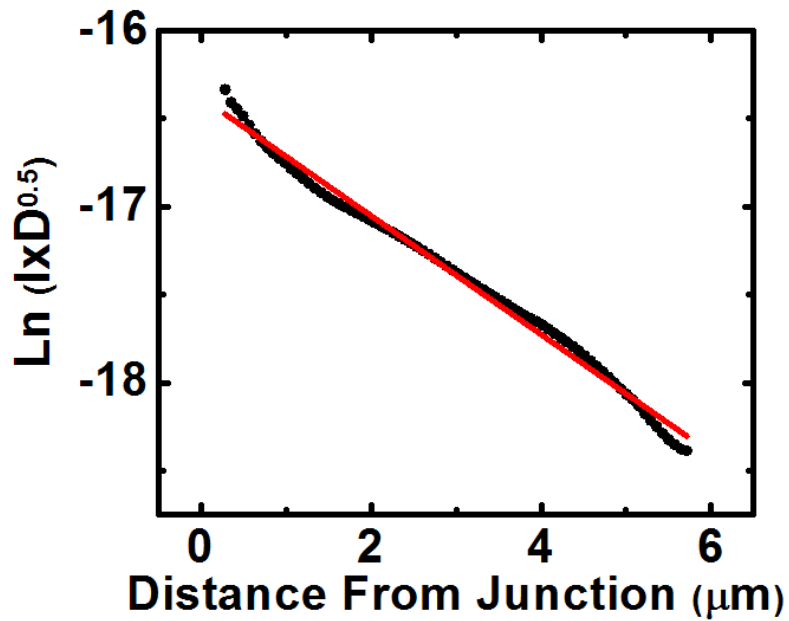
Figure 9. L_n is determined from the slope of the linear fit (red line) of the data in this graph.

Relating the diffusion coefficient, D, to temperature we get:

$$D = D_o \exp(\frac{-E_a}{k_B T}) \qquad (2.3)$$

With E_a being the activation energy of the process. Using $L = \sqrt{D\tau}$ we arrive at

Equation 2.4 relating the diffusion length to temperature by:

$$L_n = L_o \exp(\frac{-E_a}{2k_B T}) \qquad (2.4)$$

So, when $Ln(L)$ is plotted as a function of $1/2kT$ we get a slope the corresponding with

the thermal activation energy of that sample.

2.3.2 Cathodoluminscence Method

Cathodoluminescence is an optical and electrical phenomenon in which a luminescent material (semiconductor) emits light upon the impact of an electron beam produced from an electron gun. The high energy electron beam impacted onto a semiconductor will results in the promotion of electrons from the valence band to the conduction band. This movement leaves behind a hole, when the electron and hole recombine a photon may be emitted. These emitted photons can then be collected and analyzed by an optical system. Transitions in the near band edge (NBE) region of ZnO and GaN spectrum were collected through a Gatan MonoCL system integrated with the SEM [50,51].

Minority carrier lifetime is related to the lifetime of the non-equilibrium carriers in the conduction band. CL measurements were used to detect changes in carrier lifetimes with varying sample temperature as well as electron and neutron irradiation.

2.3.2.1 CL Experimental Setup

CL measurements were also performed *in situ* inside the Philips XL30 SEM. The temperatures varies in the sample were $25^{o}C$ to $125^{o}C$. The Hamamatsu photomultiplier tube is sensitive to wavelengths ranging from 185 to 850 nm. Slits sizes were kept at 4.5 mm.
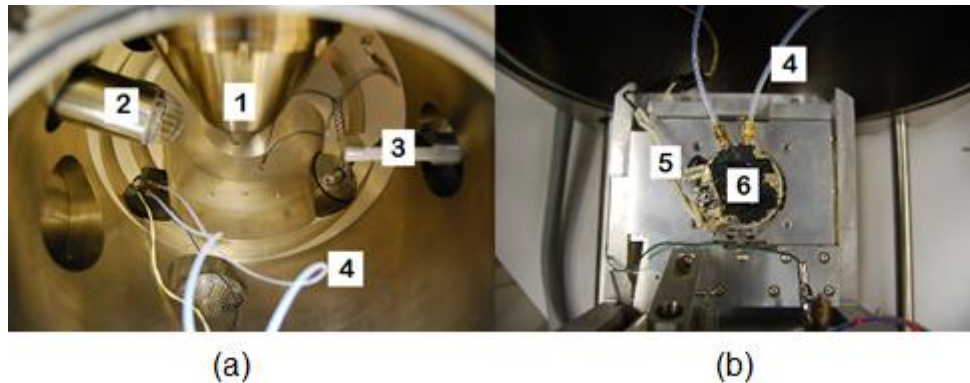
Figure 10. Inside the vacuum chamber of the SEM. (a) The electron gun (1), secondary electron collector (2), light guide (3) and plastic hoses (4) through which liquid nitrogen is passed through in order to cool the sample. (b) This is the sample stage (6) with the computer controlled heater and platinum resistance thermometer (5) connected to it.

The CL experimental set up is integrated with the SEM as seen in Figure 10. The monochromator is on the right hand side of the SEM and houses the mirrors and the diffraction grating system. Located on the right of the monochromator is the Hamamatsu photomultiplier tube. For each specific wavelength a PC is used to record the intensity of light by number of counts.

On the light guide there is a parabolic mirror which collects the emitted light from the samples. A hole is cut in the middle of the mirror to allow for the electron beam to reach the sample when the mirror is over the sample. The mirror is positioned a specific working distance, usually a few millimeters, from that sample which is optimized with Back-Scattered Electrons (BSE) for maximum intensity so that its focal length coincides with the sample. The focus size is normally in tens of microns. The light collected from this focal point comes from a parallel beam through the hollow waveguide tube and focused onto the entrance slits of the monochromator, as shown in Figure 11. The

27

electron beam may be used in spot or line scan mode. New areas are sampled after each temperature measurement is made to avoid influence from electron irradiation on that area.
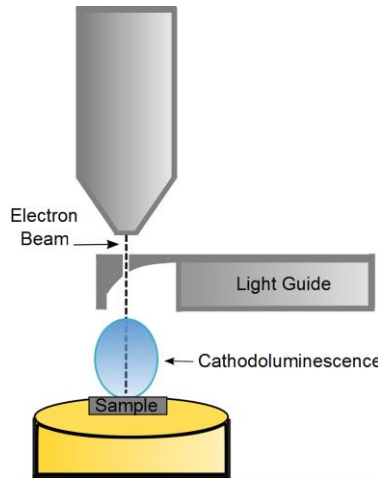
Figure 11. Diagram of the Cathodoluminescence method including the sample, light guide and electron beam.

2.3.2.2 Determining Thermal Activation Energy

Determining the thermal activation energy by use of the CL measurements is similar to the way in which the diffusion length is used to calculate the thermal activation energy using the EBIC technique. CL peak intensity, I_{CL}, of Near Band Edge (NBE) luminescence decays systematically with increasing temperature. Since CL intensity is proportional to the rate of recombination, as the intensity decreases it is shown that the number of recombination events also decreases. Also, since the intensity is inversely proportional to the lifetime of carriers in the band, the decay of I_{CL} indicates the increase

of τ with temperature. This follows in an exponential relationship represented in this Equation 2.5;

$$I_{CL} = \frac{A}{(1 + B exp(-\frac{\Delta E_a}{kT}))} \qquad (2.5)$$

Where A and B are scaling factors, ΔE_a is the activation energy, k is the Boltzmann constant and T is temperature [52].

2.4 Electron injection and Forward Biasing

The injection of electrons can be achieved by either applying a forward bias to the p-n junction to inject the electrons or by using the SEM electron beam in line scan mode to continuously irradiate the sample [53]. For EBIC measurements of electron injection the temperature dependent measurements of the diffusion length are used to calculate the activation energy through rate, R. Rate, R, is the change of L_n with the duration of electron injection, t [54]. It can be seen that the diffusion length, L_n, increases with electron injection duration. Based on previous experiments we know that at some point in time the growth of L_n will saturate and plateau, therefore only the linear portion of the growth of L_n is used in the calculation of the rate, R. Differentiating Equation 2.4 with respect to t gives [54]:

$$R = \frac{dL_n}{dt} = \exp(\frac{-E_{a1}}{2k_BT})\frac{dL_0}{dt} \qquad (2.6)$$

Then, the L_0 dependence on the duration of electron injection is:

$$\frac{dL_0}{dt} = R_0 \exp(\frac{E_{a2}}{k_B T}) \tag{2.7}$$

The activation energy E_{a1} is due to temperature dependence while E_{a2} is due to electron injection duration. With the assumption that both E_{a1} and E_{a2} are similar in value and representatives of the same process, they can be set equal to each other and the rate becomes:

$$R = R_0 \exp(\frac{E_a}{2k_B T}) \tag{2.8}$$

The 2kT factors in both the electron-induced effect on R ($\propto \exp(\Delta E_a/kT)$) and its temperature dependence ($\propto \exp(-\Delta E_a/2kT)$) [55]. Focusing on the linear part of the data the activation energy is found by rearranging in an Arrhenius graph form:

$$\ln\left(\frac{R}{R_0}\right) = \frac{E_a}{2k_B T} \tag{2.9}$$

From here, the activation energy is shown to be found from the slope of the linear relationship of the Arrhenius graph.

The activation energy of the irradiation-induced process can be determined from the temperature dependence of R as seen in Equation 2.8. Since this equation accounts for two effects that are generally assumed to be equal we can also separate the two components and arrive at this equation [55]:

$$R = R_0 \exp(\frac{E_{a,I}}{k_B T})\exp(-\frac{E_{a,T}}{2k_B T}) \tag{2.10}$$

Here, $\Delta E_{a,I}$ is the activation energy of electron irradiation effect and $\Delta E_{a,T}$ is the previously determined activation energy of thermally induced intensity decay.

Concerning CL measurements, a relationship can also be derived between CL intensity and duration of forward bias injection and electron injection duration. The rate of recombination is inversely proportional to the duration of irradiation. The electron lifetime τ and its diffusion length L are related in Equation 1.2. Diffusion length is proportional to the duration of electron beam injection t. Therefore [56];

$$t \sim \sqrt{\tau} \sim \frac{1}{I} \tag{2.11}$$

And;

$$I^{-1} \propto t^2 \tag{2.12}$$

Which gives;

$$\frac{1}{\sqrt{I}} = Rt \tag{2.13}$$

where R is the rate of decreasing peak intensity at a certain temperature. The rates are calculated at each temperature from the slopes of linear dependences of I^{-1} vs Irradiation duration. With the rate obtained, one can then calculate the activation energy for the effect. For temperature dependent CL measurements the rate is related to activation energy by Equation 2.8 and by the process henceforth described.

CHAPTER THREE - RESULTS

3.1 Prior State of the Art to the Present

In this section we begin with a flow chart describing the prior state of the art and the progression which led to the present research. First, we begin with GaN, which has long been compared to ZnO. The application of GaN for bipolar device technology depends on the production of p-n junctions. Functional p-n heterojunction devices have been produced but contain crystallographic defects at the interface which degrade optical and electrical properties [1]. Therefore, p-n homojunctions are more desirable. GaN and ZnO are naturally n-type, so the success of the p-n homojucntion relies on the production of high, stable and reproducible p-type doping in this material. However, possible acceptors form deep levels which have hindered production of p-type material in both GaN and ZnO [1,18]. Presently, in GaN, Mg has been the best acceptor dopant even with its drawbacks including limited solubility, compensation issues and high thermal activation energy [15]. Even with viable p-type doping, the performance of bipolar devices relies on the quality of transport properties of minority carriers. GaN and ZnO, both being direct band gap semiconductors, have a smaller minority carrier diffusion length than indirect band gap semiconductors. Therefore, it is important to study the properties of minority carrier diffusion length and lifetime as it depends on temperature and electron injection. In GaN, temperature and electron dependence on minority carrier diffusion length and lifetime was studied in prior research through EBIC

and CL measurements [14,17,54,56,57]. Using EBIC measurements they were able to observe a diffusion length increase dependent on temperature and electron injection and extract an activation energy for that process. Using CL measurements they were able to observe a decrease in intensity dependent on temperature and electron injection and extract an activation energy for that process. Both thermal and electron injection increases diffusion length and decreases CL intensity which is related to an increase in carrier lifetime. However, as the electron injection continues and the temperature is raised there is decrease in rate of diffusion length and lifetime increase. The activation energies related to these rates were extracted and compared. They were similar and attributed to the same electron injection effect. Since this effect was not seen in n-type GaN, the phenomenon was attributed to the dopant and a mechanism for this effect was produced. This effect was seen to last for several days. Also, the same electron injection effect was seen through forward biasing. Knowledge of this effect helped to produce a functional prototype which improved device performance. This path was illustrated in Figure 12.

Recent innovations in growth and doping of ZnO, in combination with its advantages over GaN, have placed a new interest in this material. ZnO advantages include lower material cost, use of wet chemical etching and the availability of large area lattice matched substrates. However, it is similar to GaN in its p-type doping difficulties [1,58]. This difficulty was recently overcome by size mismatched doping using Sb [20]. Once this p-type conductivity is achieved it is necessary to study the properties of minority carrier diffusion length and lifetime as it depends on temperature

33

and electron injection as was done in GaN [11,12,16,55,59]. In this research we begin with a temperature dependent measurement of the minority carrier diffusion length in the Sb doped p-type region of a ZnO p-n homojunction [42]. This was observed through EBIC measurements and an increase, similar to the one seen in GaN, was observed [15,42]. We expand the research to ZnO p-n junctions made from nanowires. Thermal and electron irradiation dependence on the minority carrier diffusion length was observed through EBIC and CL measurements [41]. We see an increase in minority carrier diffusion length as a result of temperature and electron injection similar to GaN [15,57]. We also observe a decrease in CL intensity as a result of temperature and electron injection also similar to GaN studies [56]. The increase in diffusion length and decrease in CL intensity had diminished rates as the temperature was increased as seen in GaN. The activation energies for this effect using EBIC and CL measurements were similar to each other. However, they were different than the activation energy for this effect in GaN [14,17,54,56,57]. This is expected since the different dopant produce different energy level defects for each material. From there, forward electron injection bias and temperature dependence was also studied for ZnO p-type Sb-doped nanowires [41]. A similar dependence was seen. Also, studies for n-type ZnO revealed carrier lifetime improvement through temperature and electron irradiation observed through CL measurements [40,58]. This was due to different defects located in the n-type ZnO. ZnO's path is shown in Figure 13.

Details, explanations and implications of these experiments are given in the following sections.
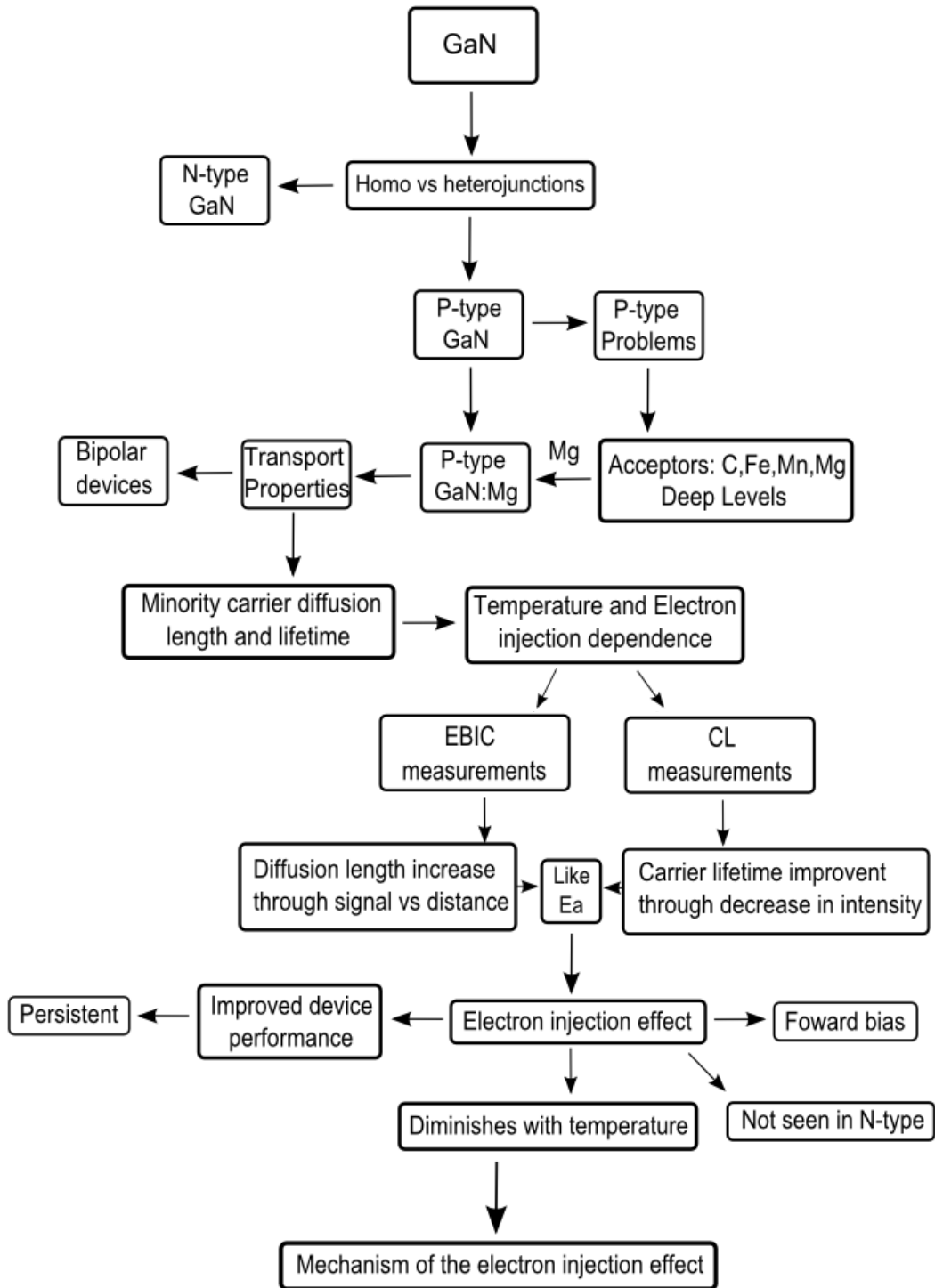
Figure 12. GaN prior state of the art.
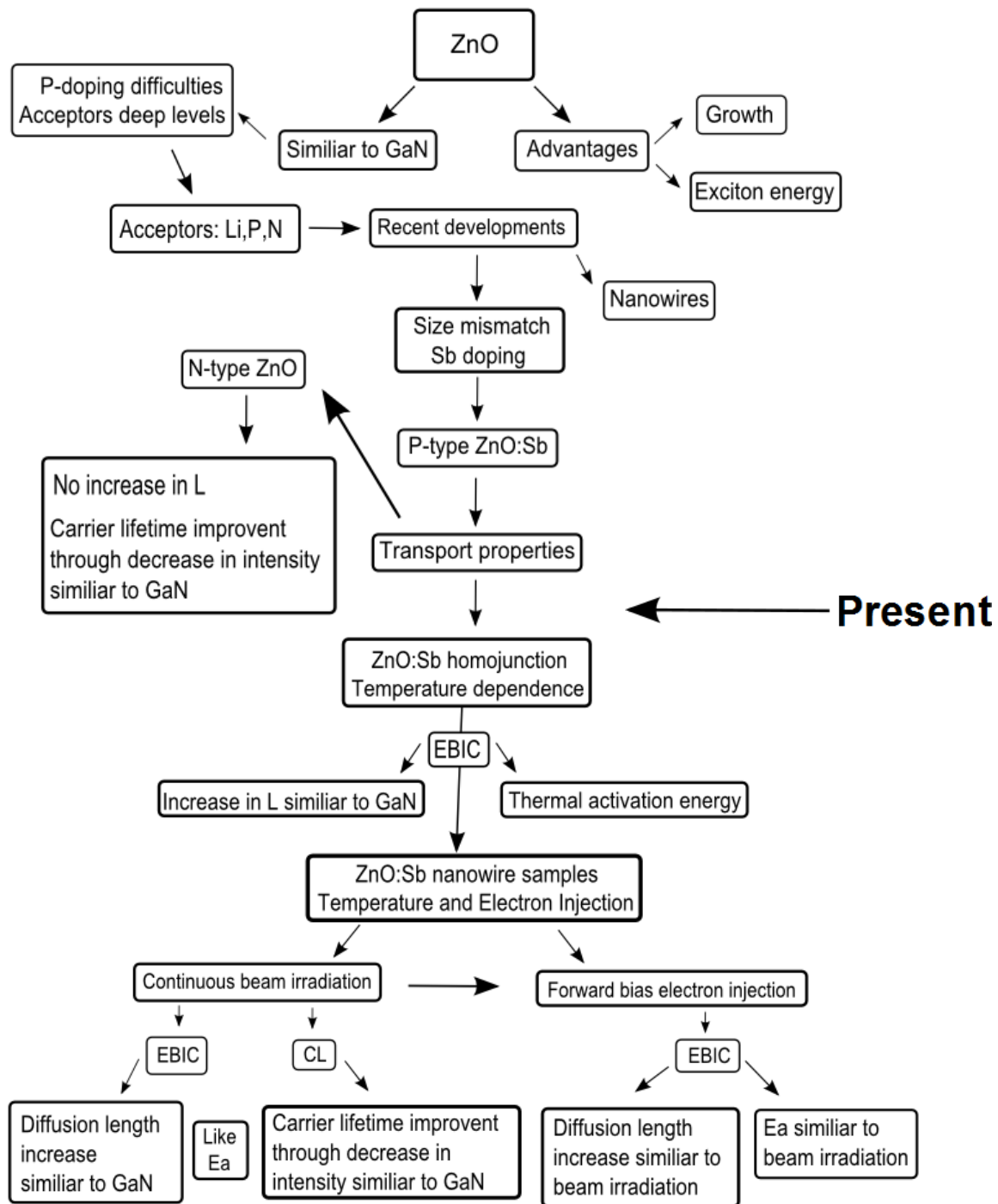
Figure 13. ZnO prior state of the art to present.

3.2 Studies of Temperature Dependence

3.2.1 P-type ZnO homojunction doped with Sb

ZnO p-n homojunctions were formed by growing a n-type ZnO:Ga layer on a highly resistive (200 Ω cm) p-Si substrate, followed by a p-type ZnO:Sb layer by MBE method shown in Figure 14(a). Ohmic contacts Au/NiO and Au/Ti were formed on p-ZnO and n-ZnO, respectively. Hall effect measurements showed that the Ga-doped ZnO layer had an electron concentration, mobility, and resistivity of 2.8×10^{19} cm^{-3}, 8.7 cm^2 V^{-1} s^{-1}, 0.02 Ω cm, respectively. The Hall effect measurements were carried out on a n-type layer after the top p layer was etched off. Therefore, surface roughness due to etching and Si-substrate effect may impact the obtained values of carrier concentration and mobility in n-ZnO. Also, very large density of ionized donors in n-ZnO may cause stronger impurity scattering in the n layer and, as a result, lower carrier mobility. Figure 14(b) shows a typical current-voltage I-V curve of ZnO p-n junction diode in a semilogarithmic scale. In the figure, the turn-on voltage has been determined to be more than 3.4 V. N-n junctions may also have rectifying characteristics however their turn on voltage would be less than 1.7 V assuming good Ohmic contacts. Therefore, it is confirmed that the diode under test is a p-n rather than a n-n junction. Temperature dependent EBIC measurements were collected from the ZnO p-n homo-junction in the p-type region.
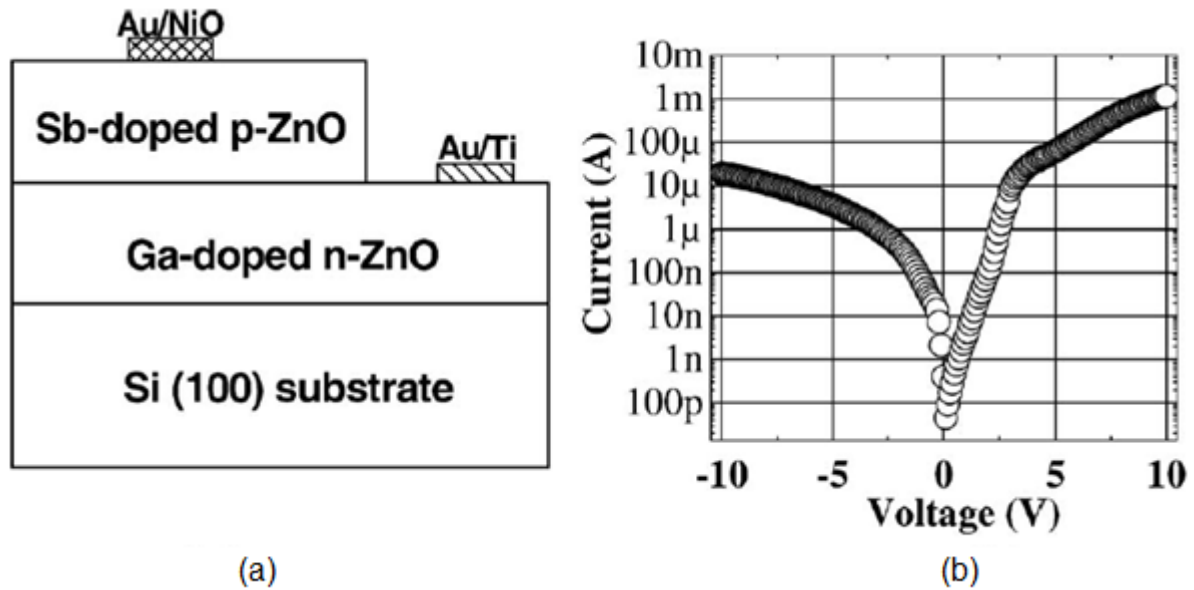
Figure 14. (a) Architecture of ZnO p-n homojunction. Metal thickness for contact layers are as follows: Au/NiO, 300/30 nm, Au/Ti 150/30nm ZnO *p-* and *n*-epitaxial layers are 425 nm thick each. Si substrate (shown not to scale) is *p* type with resistivity of ~200 Ω cm. (b) *I-V* curve for ZnO *p-n* junction at room temperature [42].

3.2.1.1 Minority Carrier Transport Properties

The EBIC technique is dependent on the non-equilibrium carriers generated in semiconductors under the influence of electron beam irradiation and their resulting separation by the built in field of the p-n junction or Schottky diode. As majority carriers are swept away from the region of the p-n junction's built-in field localization, the minority ones instead build up and strengthen the magnitude of the overall electric current (i.e., EBIC). By measuring the EBIC dependence on the distance from the p-n junction and with the use of Equation 2.1, the minority carrier diffusion length, *L*, can then be extracted from the EBIC line scan.
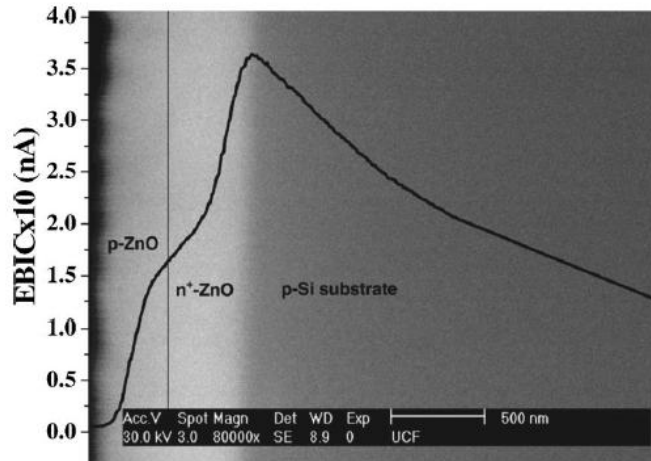
Figure 15. Secondary electron image of device structure cleaved perpendicular to the growth plane and the superimposed EBIC line scan [42].

An exponential decay of the EBIC signal was found in the p-ZnO layer which allowed for the extraction of the minority carrier diffusion length from the EBIC line scan shown in Figure 15. Minority carrier diffusion length measurements were performed *in situ* in Phillips XL30 scanning electron microscope under a 30kV electron beam accelerating voltage on the structures cleaved perpendicular to the growth plane.

The temperature was then varied from 25°C to 125°C and EBIC line scan measurements were conducted at each temperature in different locations. It is important to mention that the diffusion length in p-type ZnO nanowires is several times larger than that seen in epitaxial p-ZnO:Sb layers. While the EBIC signal in p-ZnO layer exhibits an exponential decay to the left from the p-n junction interface, the electron beam induced current in the n-ZnO layer increases with SEM electron beam moving to the right of the p-n junction toward Si substrate (ideally the EBIC signal should decay to zero at n-ZnO/

Si interface). The latter increase is related to the additional nonequilibrium electron collection from the substrate. Although the Ohmic contacts to p- and n-ZnO layers are used for EBIC measurements, the electrons from Si substrate, due to their very long diffusion length (~100 µm), are swept by the built-in field of the space charge region at n-ZnO/ Si interface (this region is predominantly located in the highly resistive Si substrate) and are collected at the contact to n-ZnO layer, thus, contributing to the EBIC signal and making determination of minority carrier diffusion length in n-ZnO impossible under the present configuration. On the contrary, a pronounced exponential decay of the EBIC signal in p-ZnO layer allows extraction of minority carrier diffusion length from the EBIC line scan [42].

Values of electron diffusion length in the p-type region of ZnO p-n homo-junction were averaged and plotted in relation to its temperature dependence shown in Figure 16. Equation 2.1 was used to extract the minority carrier diffusion length, *L*, from the line scan.
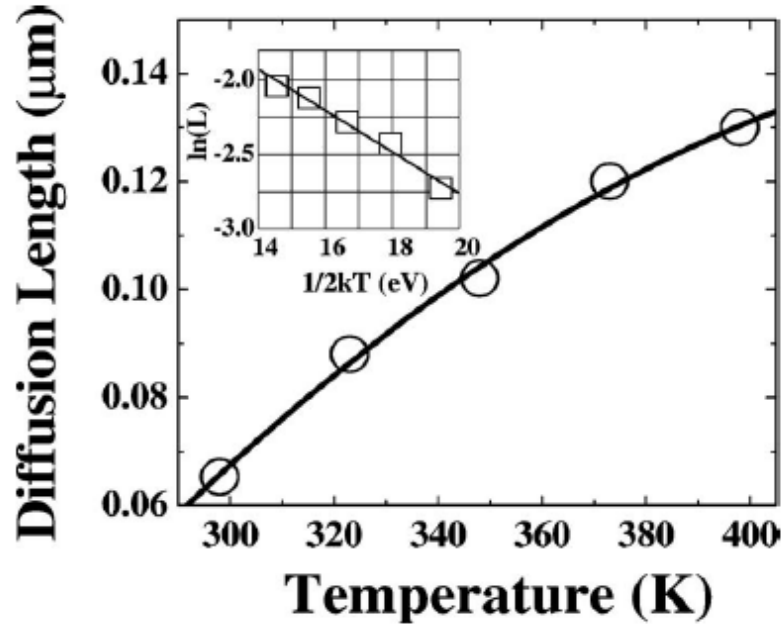
Figure 16. The diffusion length (mean values) of the minority electrons as a function of temperature (open circles). Inset: Arrhenius plot of the same data yielding activation energy of 145±10 meV [42].

The value of L was seen to increase exponentially as the temperature increased. This behavior was then modeled by the Equation 2.4. From the inset Arrhenius plot in Figure 16, the value of the thermal activation energy was determined to be 145±10 meV.

The thermal activation energy, $E_{a,T}$, represents carrier delocalization energy and as a parameter for determining the increase of the diffusion length due to the reduction in recombination [75]. Previous CL studies on ZnO:Sb epitaxial layers suggest that the recombination route of nonequilibrium carriers emerge from transitions to a deep, neutral acceptor level (e,A^0) [11]. When the sample is heated, the fraction of acceptors that are ionized are also increased. This in turn reduces the concentration of A^0 which hinders the recombination rate. Equation 1.2 shows the diffusion length, L, in correlation

with the diffusion coefficient, D, and lifetime, τ. Therefore, as the recombination rate decreases, the lifetime of the minority electrons in the conduction band increases. This leads to a greater diffusion length. The 145±10 meV value of the activation energy correlated nicely with previous CL studies [11,42].

3.3 Studies of the Effects of Electron Injection and Temperature Dependence

3.3.1 Electron irradiation of p-type ZnO nanowires doped with Sb

P-type ZnO nanowires doped with Sb were grown using a thermal scientific quartz furnace system. The zinc source was placed in the center of the quartz tube, while Sb_2O_3 powder was placed 5 cm from the source, which was 10 cm away from the undoped ZnO film grown on a sapphire substrate by plasma assisted molecular beam epitaxy. The furnace was flown continuously by nitrogen while the whole system was heated up to 650 °C. Then, an argon/oxygen (1000:5) mixture was introduced into the quartz tube for ZnO nanowire growth for 30 min. A section of the ZnO film and nanowires was covered by an Ag contact. Electrical transport properties of ZnO nanowires were obtained using Field Effect Transistor (FET) measurements. Hole concentration of 4.5×10^{17} to 2.5×10^{18} cm^{-3} were calculated. The carrier mobility was determined to be 0.005 to 0.03 cm^2/Vs [61]. The mobility value here is actually the low bound limit of the real mobility; this is due to the non-ohmic contacts located between the metal and nanowire contributing to a large resistance. Temperature and electron injection dependent EBIC measurements were collected from the sample.

3.3.1.1 Minority Carrier Transport Properties

The EBIC signal was recorded within the nanowire layer, beginning from the n-ZnO/p-ZnO interface, on a sample cleaved perpendicular to the plane of growth. In Figure 17, one can see the superimposed EBIC line-scan signal following a path of exponential decay in the p-type ZnO nanowire region. The area of effect is over multiple nanowires as a result of the size of the electron beam and the resulting EBIC signal is, therefore, an average over several nanowires. All experiments were conducted *in-situ* in a Philips XL30 Scanning Electron Microscope (SEM) under an accelerating voltage of 20kV.
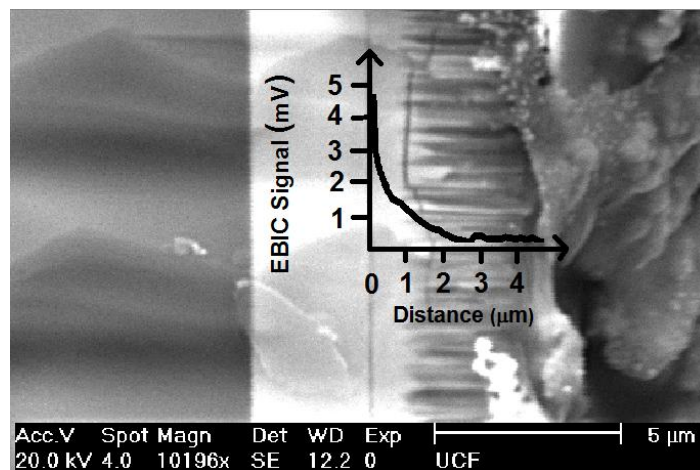
Figure 17. Secondary electron image of the samples cross section taken perpendicular to the growth plane. From left to right: sapphire substrate; n-ZnO film; p-ZnO (nanowire layer); and Ag-epoxy layer (used for a contact). EBIC measurements were taken from the n-ZnO film/p-ZnO nanowire interface. Superimposed: exponential decay of EBIC signal versus the beam-to-barrier distance.

Line scans of 24 seconds each were performed on the sample while the EBIC measurements were collected and used to extract a diffusion length. Temperatures were varied from 25°C to 125°C. At each temperature the electron beam was repeatedly scanned across the same location for a total of 2000 seconds. Diffusion length measurements were taken at 500 second increments. For each temperature a new location was examined.

As the temperature was raised in the sample the diffusion length was increased. The relationship between diffusion length, L, and temperature is shown in Figure 18. The value of L increases exponentially with temperature increase; this is fitted to Equation 2.4. The thermal activation energy was found from the Arrhenius plot to be 112±3 meV.
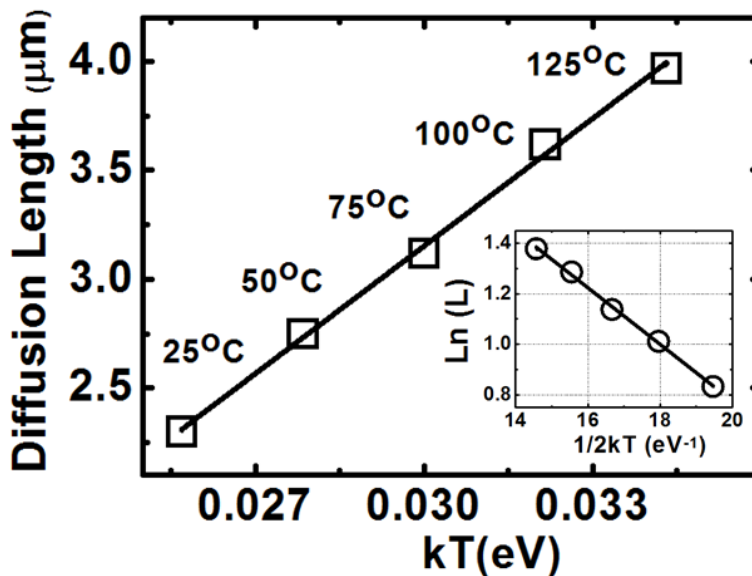
Figure 18. Dependence of diffusion length on temperature in the nanowire p-ZnO region. Insert: Arrhenius plot for L vs. T dependence resulting in a value for activation energy of 112±3 meV.

This thermal activation energy represents carrier delocalization energy and determines the increase in diffusion length due to reduction in recombination efficiency as seen in p-type region of the ZnO p-n homojunction discussed previously.

Continuous irradiation of the sample by the SEM electron beam was shown to also produce an increase in L. In Figure 19, the rate of the diffusion length increase is reduced with increasing temperature. The irradiation induced growth rate of L is diminished with increasing temperature and by using Equation 2.10, we determined an activation energy for this dependence. Plugging in the thermal activation energy of 112 ± 3 meV we found an activation energy for the electron effect to be 233 ± 10 meV.
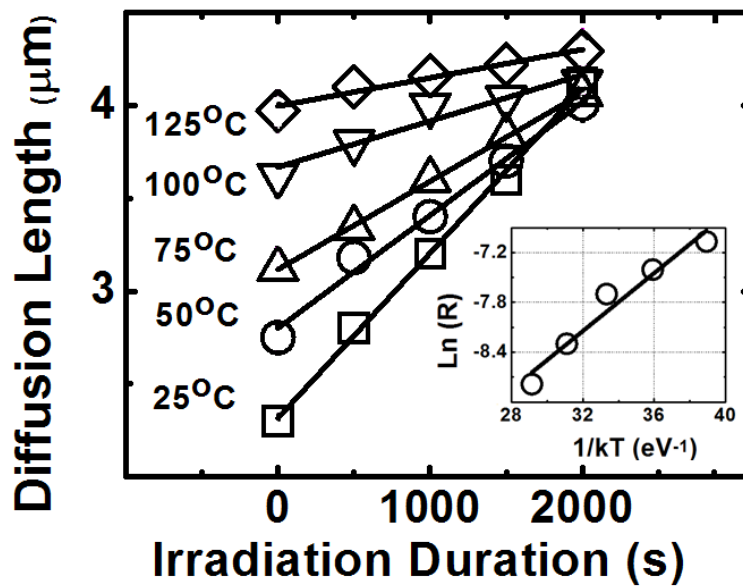
Figure 19. Dependence of diffusion length on electron beam in temperature in the nanowire p-ZnO region. Insert: Arrhenius plot for L vs. 1/kT dependence producing a value for the activation energy of 233 ± 10 meV.

The irradiation induced increase of L is expected to be due to the non-equilibrium electron created by the electron beam being trapped by the neutral acceptor levels ($A^0 +$ $e^- \rightarrow A^-$). This excludes this level as a pathway to recombination and in turn reduces the recombination rate which leads to longer lifetime for electrons in the conduction band. The concentration of neutral levels is reduced as excitation proceeds and the diffusion length steadily rises. However, the rate of the increase of L is reduced with increasing temperature. This happens because as the temperature is increased, the energy of the electrons is also increased and as the carriers gains more energy they can escape more successfully from the traps. The activation energy of this electron effect is 233±10 meV. This suggests that the level responsible for this increase seen in L is due to a Sb_{Zn}-$2V_{Zn}$ acceptor complex.

3.3.1.2 Optical Properties

With minority carrier diffusion length begin related to the lifetime of non-equilibrium carrier in the conduction band, cathodoluminescence measurements provide a useful method to monitor changes in carrier lifetime due to temperature and irradiation.

CL measurements were conducted *in-situ* in a Philips XL30 Scanning Electron Microscope (SEM), integrated with a Gatan MonoCL3 CL system under an accelerating voltage of 20kV. An area of 2 by 2 µm was selected and used to take an average value

of the CL intensity over multiple nanowires located in the p-type region of Figure 17. The CL spectrum was found in the vicinity of the NBE transition at 385 nm (3.33 eV).

Temperature dependent measurements were then conducted for temperatures ranging from 25°C to 125°C and over wavelengths ranging between 260 and 420 nm. For each temperature a new area was selected. The sample was then irradiated by continuous electron beam impaction up to 1500 seconds while measurements were taken intermittently at 0, 500, 1000 and 1500 seconds. This was also done for temperatures ranging from 25°C to 125°C. For each temperature a fresh area was also chosen to avoid contamination by the electron beam.

As the temperature was raised in the sample a decrease in CL NBE intensity of the spectra can be seen in Figure 20. The peak intensities of each spectrum at each temperature were averaged and fitted in accordance with Equation 2.5 which yielded a thermal activation energy of 115±10 meV.
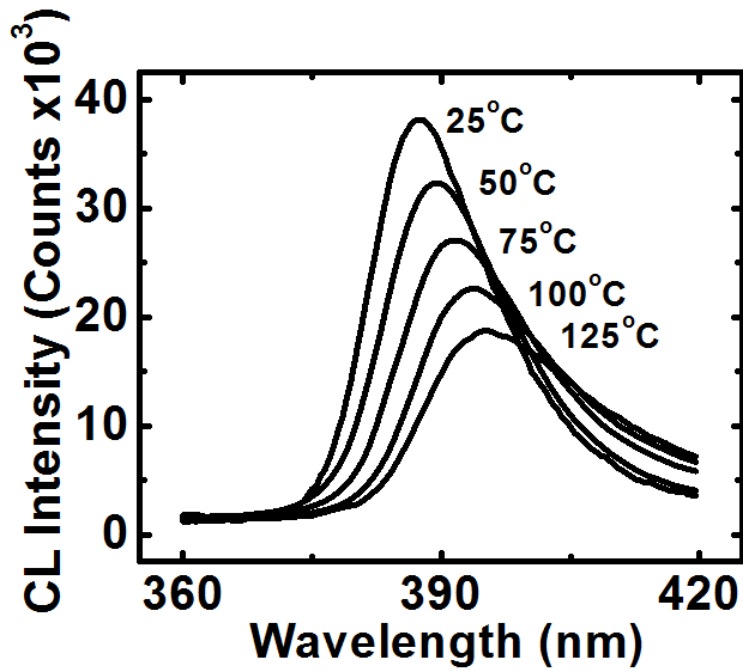
Figure 20. Cathodoluminescence spectra measurements for various temperatures.
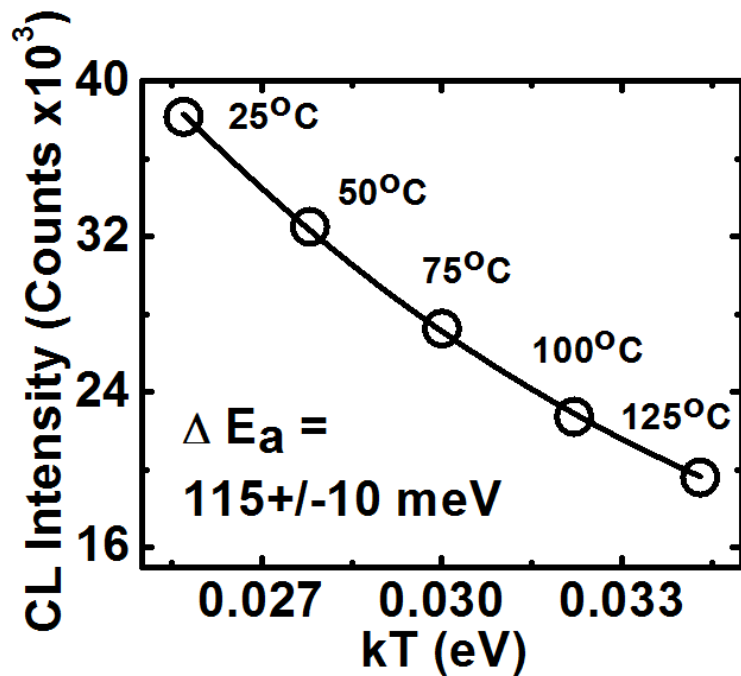
Figure 21. Decay of CL peak intensity with temperature fitted to Equation 2.5. A thermal activation energy is extracted as 115±10 meV.

From Figure 21 it is shown that the peak intensity systematically decays with increasing temperature demonstrating that the rate of recombination event decreases. The thermal activation energy of 115±10 meV is similar to that of the temperature dependent EBIC measurements, 112±3 meV, which suggest that a similar process is responsible for both the increase in diffusion length and the decay of CL intensity. When non-equilibrium electron-hole pairs are generated by the electron beam they will eventually recombine with each other. Since the hole capture cross-section is inversely proportional to temperature [60.62], the frequency of the recombination events, represented by CL intensity here, decreases with temperature.

CL intensity was seen to decay as a result of electron irradiation duration. The decay of the NBE intensity at 25°C with increasing irradiation duration can be seen in Figure 22. The rates, R, are calculated from the slopes of Figure 23 for each temperature. By fitting the data rate R and the corresponding temperature T to Equation 2.10, we can extract an electron irradiation activation energy of 212+/-15 meV as shown in Figure 23. This is similar to the value of 233±10 meV which came from the electron irradiation activation energy EBIC measurements for the increase in L.
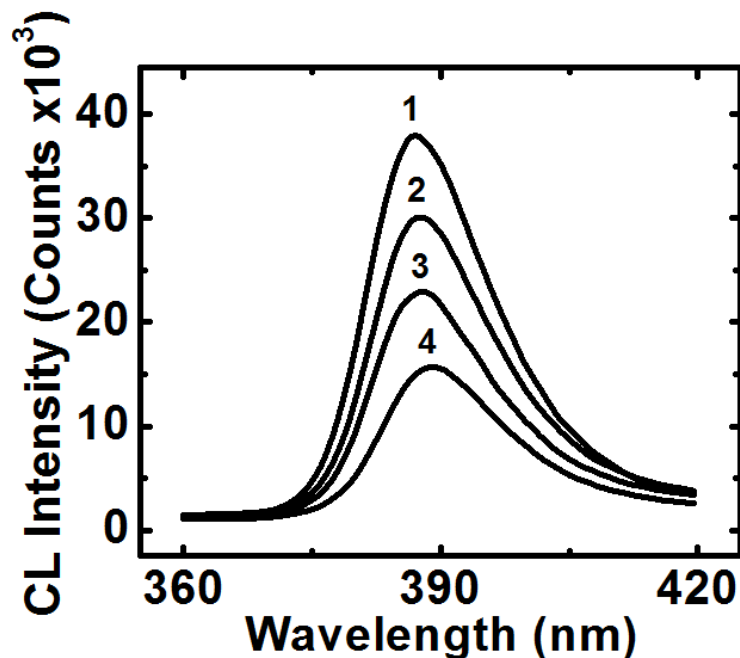
Figure 22. Decay of CL intensity with increasing electron irradiation duration. From top to bottom: spectra 1-4 correspond to irradiation under the SEM electron beam for 0, 500, 1000,1500 seconds respectively.
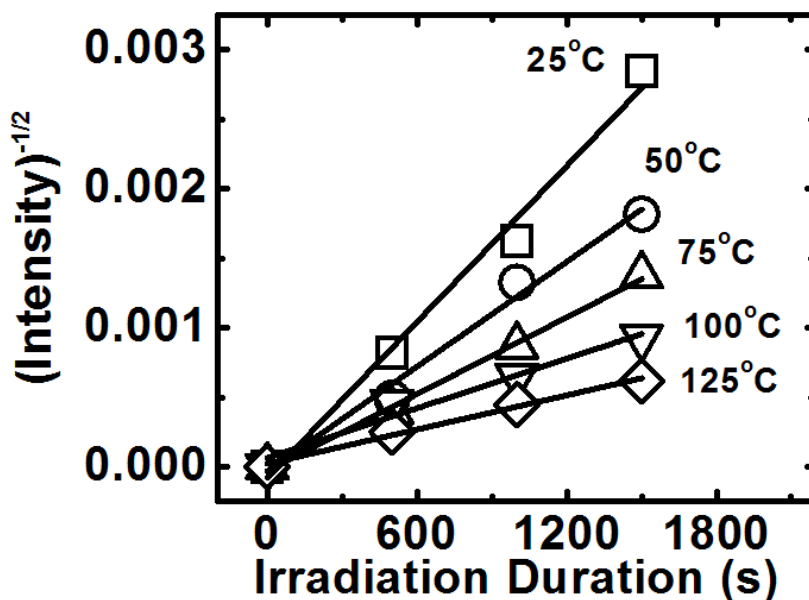
Figure 23. Relationship between intensity and irradiation duration for various temperatures. Using a linear fit of Equation 2.13 the rates were obtained as slopes of these lines. The values are: $R_{25^{o}C}$ $1.87 \times 10^{-6} s^{-1}$, $R_{50^{o}C}$ $1.26 \times 10^{-6} s^{-1}$, $R_{75^{o}C}$ $9.2 \times 10^{-7} s^{-1}$, $R_{100^{o}C}$ $5.95 \times 10^{-7} s^{-1}$, $R_{125^{o}C}$ $4.1 \times 10^{-6} s^{-1}$.
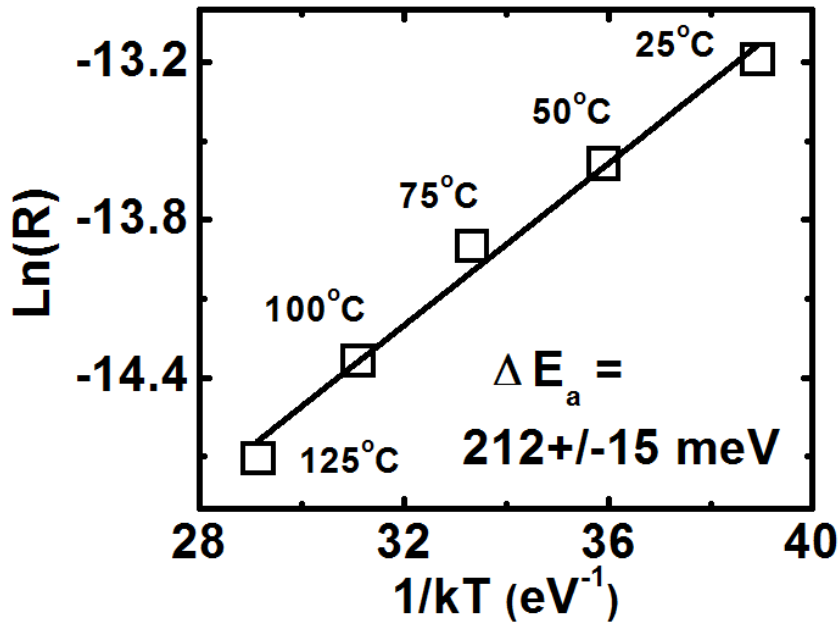
Figure 24. Arrhenius plot of logarithm of rate R vs. (1/kT). Using the linear fitting of Equation 2.10, we obtained the activation energy of 212±15 meV.

A decreasing rate can be seen with increasing temperature and suggests that a thermally activated process, opposing the lifetime increase induced by electron irradiation, exists simultaneously. This is due to the process described for the EBIC measurements of the L increase due to electron irradiation. This process is a result of trapped electrons overcoming an energy barrier and reestablishing the recombination pathway while inhibiting the increase in electron lifetime. The electron irradiation activation energy of 212±15 meV is close to value of 233±10 meV which came from the electron irradiation activation energy EBIC measurements for the increase in L, this suggests that the level responsible for both is due to a Sb_{Zn}-$2V_{Zn}$ acceptor complex [20].

3.3.2 Forward bias injection of p-type ZnO nanowires doped with Sb

Experiments were carried out on a sample that contained *p*-type Sb-doped nanowire layers. The sample consists of a very thin MgO buffer layer and a 2 μm-thick, undoped n-type ZnO epitaxial film grown on a Si (100) substrate by Molecular Beam Epitaxy (MBE) under a growth temperature of 450°C. The sample was then transferred to a Thermal Scientific quartz tube Chemical Vapor Deposition (CVD), in which the nanowires were grown. During the nanowire growth, the temperature was kept at 600°C. The result was a p-type ZnO nanowire layer measured to be about 5 μm thick. The top surface of nanowire layer was then covered with a silver paste for contacting purposes. Temperature and forward bias electron injection dependent EBIC measurements were conducted on the sample.

3.3.2.1 Minority Carrier Transport Properties

The EBIC signal was recorded within the nanowire layer, beginning from the n-ZnO/p-ZnO interface, on a sample cleaved perpendicular to the plane of growth. In Figure 25, one can see the superimposed EBIC line-scan signal following a path of exponential decay in the p-type ZnO nanowire region. All experiments were conducted *in-situ* in a Philips XL30 Scanning Electron Microscope (SEM) under an accelerating voltage of 20kV.
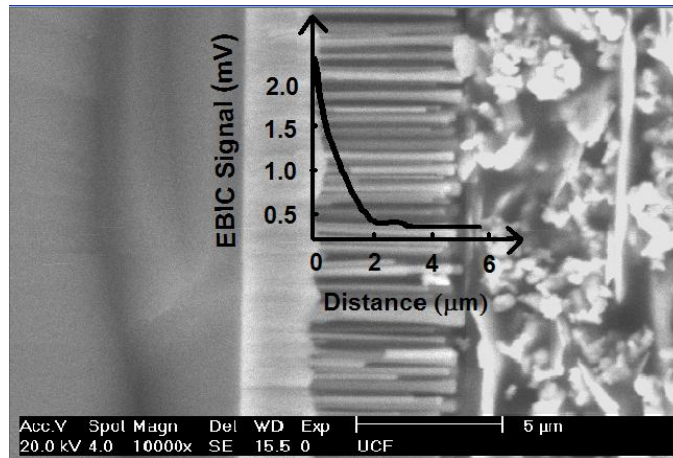
Figure 25. Secondary electron image of the samples cross section taken perpendicular to the growth plane. From left to right: silicon substrate; n-ZnO film; p-ZnO (nanowire layer); and Ag-epoxy layer (used for a contact). EBIC measurements were taken from the n-ZnO film/p-ZnO nanowire interface. Superimposed: exponential decay of EBIC signal versus the beam-to-barrier distance [41].

Temperature dependent diffusion length measurements were taken at temperatures ranging from $25^{o}C$ to $75^{o}C$ by EBIC line scans of 24 seconds. New locations for the scan were chosen for each temperature. A forward bias was then applied to the p-n junction between the p-type ZnO nanowires and the n-type ZnO film resulting in a current of ~ 5 mA. After the initial line-scan (24s), EBIC measurement, and extraction of diffusion length L, the forward bias injection was continued by applying 12V for a total of 600 seconds in 100 second increments. This process was repeated at temperatures adjusted to 25, 45, 55 and 75 °C. The electron beam was turned off while applying forward bias and a new region was selected at each temperature to diminish the effect of electron beam irradiation on minority carrier transport.

53
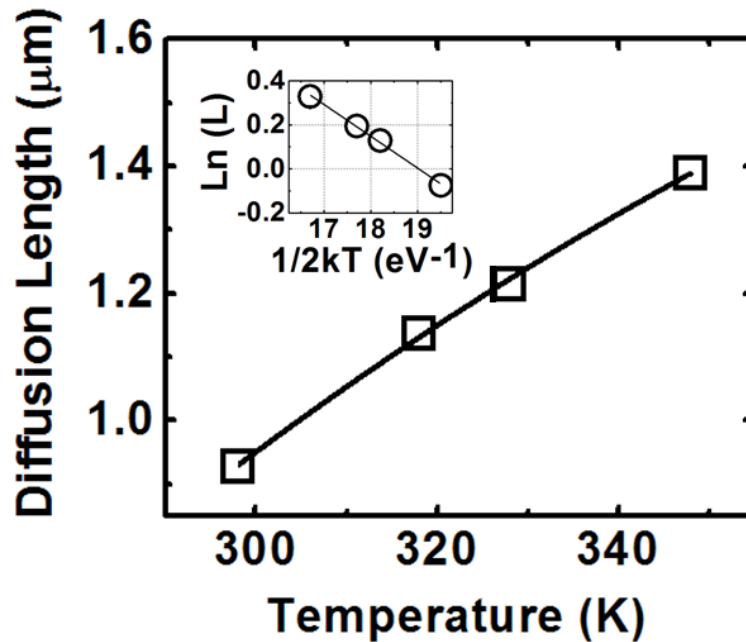
Figure 26. Dependence of diffusion length on temperature in the nanowire p-ZnO region. Insert: Arrhenius plot for *L* vs. T dependence resulting in a value for activation energy of 144±5 meV [41].

As the temperature was raised in the sample the diffusion length was shown to be increased. The relationship between diffusion length, *L*, and temperature is shown in Figure 26. The value of *L* increases exponentially with temperature increase; this is fitted to Equation 2.4. The thermal activation energy was found from the Arrhenius plot to be 144±5 meV [41].

This energy likely represents carrier delocalization energy and determines the increase of the diffusion length due to the reduction in recombination efficiency [60]. This is similar to what was seen in the p-type region of the ZnO p-n homojunction as well as the p-type region of the ZnO nanowire samples mentioned previously.

The application of a forward bias to the p-n junction of the sample resulted in an increase in the minority carrier diffusion length. From Figure 27, the rate of the diffusion length increase is shown to become reduced with increasing temperature. Accounting for rates, R, at various temperatures, which can be obtained from the dependences of L on forward bias injection duration, E_{fbi} can be calculated from Equation 2.10 using a linear fitting of ln(R) vs. 1/kT, as shown in the inset of Figure 27. E_{fbi} was found to be 217±20 meV. This is in good agreement with our previous work on p-type ZnO nanowires (233-212 meV), where the impact of electron beam irradiation on minority carrier transport was studied.
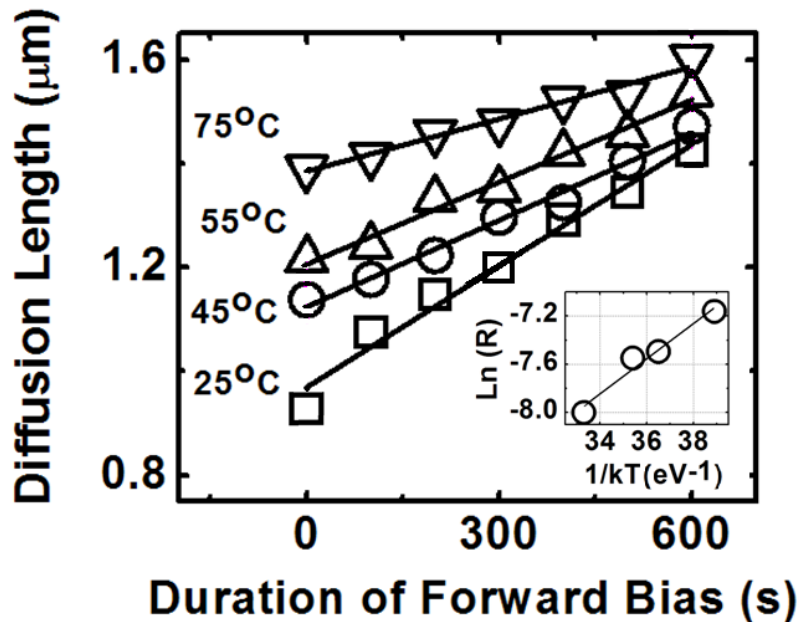
Figure 27. Linear dependence of the diffusion length on forward bias duration under increasing temperature. The rates, R, of increase of L for each temperature is obtained from the slope. Insert: Arrhenius plot for R vs. T dependence resulting in the activation energy of 217±20 meV [41].

The forward bias injection-induced increase of L suggests that it comes from a similar origin to that of the electron beam irradiation-induced increase mentioned before [41]. Also as observed before, as the temperature was raised under forward bias, a related reduction in the diffusion length growth rate can also be observed in Figure 27. This reduction in rate happens as the carriers systematically gain enough energy to escape the traps. With the forward bias injection activation energy being similar to that of the electron injected activation energy we can assume that that the level responsible for this increase seen in L is due to a Sb_{Zn}-$2V_{Zn}$ acceptor complex [20].

3.3.3 Electron irradiation of n-type ZnO

A 170-nanometer thick unintentionally doped n-type ZnO sample was grown by Molecular Beam Epitaxy (MBE) method on a silicon substrate. This sample had an electron concentration of (2-3) x 10^{17} cm^{-3}. While there have been previous reports concerning impurity activity in p-type ZnO, this experiment is geared towards impurity activity in n-type ZnO. Temperature dependent electron injection Cl measurements were collected from n-type ZnO.

3.3.3.1 Optical properties

CL measurements were conducted in-situ in a Philips XL30 Scanning Electron Microscope (SEM), integrated with a Gatan MonoCL3 CL system. To avoid electron beam penetration from the epitaxial ZnO layer to the underlying silicon substrate the

accelerating voltage was set to 5kV in the SEM. Every measurement was done on an area of the sample which had not been previously exposed to the electron beam.

Temperature dependent measurements were conducted for temperatures ranging from 25°C to 130°C and over wavelengths between 340 and 430 nm. For each temperature a new area was selected. The sample was then irradiated by continuous electron beam impaction up to 1500 seconds while measurements were taken intermittently. This was also done for temperatures ranging from 25°C to 130°C. For each temperature a fresh area was also chosen to avoid contamination by the electron beam.
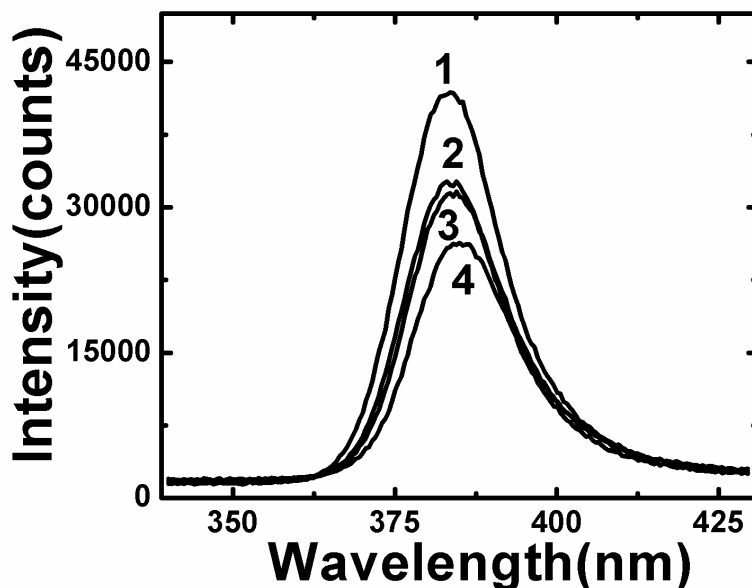
Figure 28. Cathodoluminescence measurements at room temperature. From the top to bottom: spectra 1, 2, 3, 4 correspond to irradiation under SEM electron beam for 0, 480, 600, 900 seconds, respectively [40].

The decay of the intensity of the NBE due to electron irradiation duration can be seen in Figure 28. The spectrum has a maximum peak around 377 nm corresponding to an energy of about 3.3 eV. Recombination of non-equilibrium conduction band electrons is halted by trapping the injected electrons on meta-stable defects levels in the ZnO forbidden gap. This increases electron lifetime in the conduction band and diminishes the intensity of the spectrum [40].
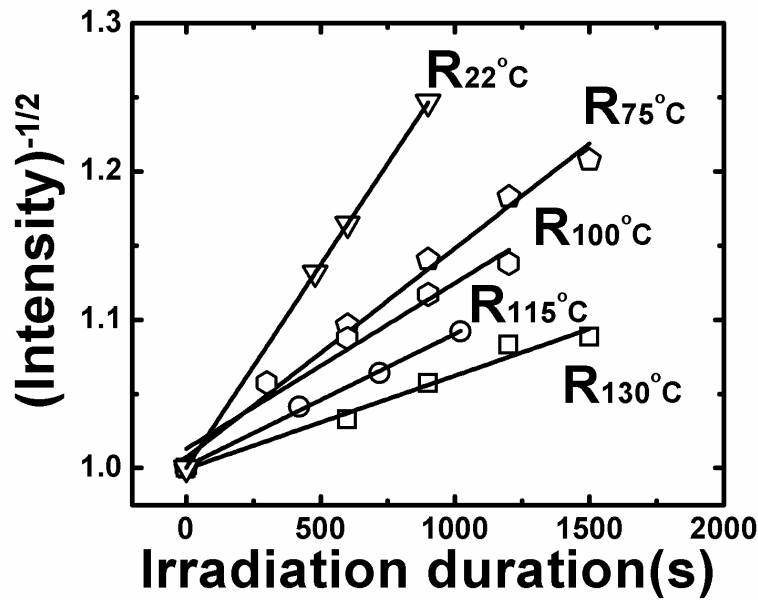
Figure 29. Relation between intensity and irradiation duration at various temperatures, with peak intensity dropping rate *R* corresponding to each temperature, respectively. The calculations are obtained using the linear fit of Equation 2.13, with R as the slopes of the lines. The values are: $R_{22^{\circ}C}$ 2.7x $10^{-4}s^{-1}$, $R_{75^{\circ}C}$ 1.4x $10^{-4}s^{-1}$, $R_{100^{\circ}C}$ 1.1x $10^{-4}s^{-1}$, $R_{115^{\circ}C}$ 8.9x $10^{-5}s^{-1}$, $R_{130^{\circ}C}$ 6.3x $10^{-5}s^{-1}$ [40].

The decay of the near-band-edge (NBE) luminescence intensity versus electron irradiation duration was shown at various temperatures in Figure 29. In Figure 29, the

intensity was normalized with respect to its initial value at each temperature. As the temperature of the sample is increased, the electron injection induced decrease of the peak intensity slows down. The rates at each temperature are calculated from the slopes of the individual lines. With the rate R obtained, one can calculate the activation energy for the electron beam-induced CL intensity change using Equation 2.8. The activation energy obtained for this sample was 259±30 meV [40].
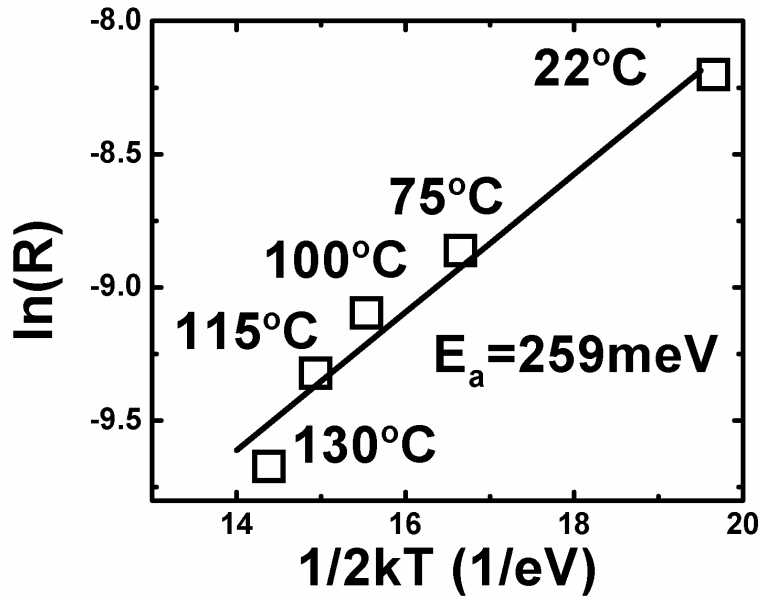
Figure 30. Arrhenius plot of logarithm of rate R vs. (1/2kT), where k is the Boltzmann constant. Using the linear fitting of Equation 2.8, we obtained the activation energy of 259±30 meV [40].

This rate decrease suggests that a thermally activated process, counter to the lifetime increase, induced by electron injection, exists simultaneously. This process can

be described by trapped electrons overcoming an energy barrier (since this process is activated by an increase in temperature) and recombining with the holes in the valence band. Then when the temperature is raised, more trapped electrons overcome the barrier, thus reestablishing the recombination pathway and slowing the increase of the electron lifetime [11,40].

The electron irradiated activation energy of 259±30 meV is in reasonable agreement with interstitial Zn (Zn_i) localization in the ZnO forbidden gap – 290meV [63]. From this we can conclude that interstitial zinc is the best candidate responsible for the observed effect. But this by no means excludes other possibilities, such as charging of grain boundaries. The grain boundaries may trap electrons in the potential wells, with holes either going over the potential barrier or tunneling through it, to recombine with these electrons. Under the SEM beam excitation, the electron pockets in the potential profile might be metastably filled, so that recombination would occur more and more via ordinary recombination centers. The competing process is the electron emission from the grain boundary potential well. The latter process becomes more pronounced as the temperature of injection increases.

3.4 Studies of the Effects of Neutron Irradiation

3.4.1 Neutron Irradiation and annealing of n-type ZnO nanostructures

ZnO nanorods were grown on quartz and Si substrates using facile and soft aqueous solution method without using catalysts, templates and seeds. The substrates

were cleaned in dilute HCL solution for 10 min followed by a rinse in de-ionized (DI) water. Then the substrates were rinsed in ethanol/acetone (1:1) mixture, DI water, and dried in nitrogen, which gave uniformly wet-able substrate surfaces. Starting materials were analytic-grade zinc sulfate and ammonia solutions. Substrates were then placed into the aqueous solution on a hot plate kept at 90^0C for 15 minutes. The substrates were washed with DI water and the product dried in 100^0C air for 10 min. Phase purity and composition of the ZnO nanorods were examined by X-ray diffraction (XRD) using a Rigaku 'D/B max' X-ray diffractometer equipped with graphite monochromatized CuKα radiation (λ=1.54178 Angstroms) and operating conditions of 30mA and 40kV at a scanning rate of 0.02^0/s in the 2θ range of 10-90^0. Bulk ZnO hydrothermally-grown crystals were obtained from Air Force Research Lab, Hanscom AFB MA courtesy of Dr. Davis Bliss.

Three of the four bulk monocrystal ZnO samples were irradiated in the central vertical port of the University of Florida Training Reactor (UFTR, 5×10^{13} n/cm^2 –sec thermal neutron flux) for 1, 10 and 20 hours. The fourth sample was kept as a control. The neutron irradiated ZnO samples and the control ZnO sample were annealed at a temperature of 600^0C for ~ 1 hour in flowing argon.

Hall measurements were done on the bulk samples to gage the effects of dose on resistance, mobility and carrier concentration before and after annealing. Using the Van der Pauw technique the experiment was conducted at room temperature. Gold-platinum contacts were sputtered on each sample, then, indium solder was used to

attach copper wires from the contacts to the four poles of the Hall setup. Contacts were removed by etching in nitric acid before annealing took place.

The nano-structured ZnO and control bulk samples were irradiated by neutron doses 1.5×10^{14}; 6×10^{14}; 1.5×10^{16} n/cm^2 in the vertical port of the University of Florida Training Reactor. Cathodoluminescence measurements were conducted at 300K in-situ in a Philips XL30 Scanning Electron Microscope (SEM), integrated with a Gatan MonoCL3 CL system excited by the 20 kV electron beam.

3.4.1.1 Neutron Irradiation Process

Six isotopes of Zn and three isotopes of O exist in nature and they are $^{64}Zn(48.6,0.74)$, ^{65}Zn (27.9,0.9), $^{66}Zn(4.1,6.9)$, $^{67}Zn(18.8,0.87)$, $^{68}Zn(18.8,0.87)$, $^{70}Zn(0.6,0.0091)$, $^{16}O(99.78,1.9 \times 10^{-4})$, $^{17}O(0.038,5.4 \times 10^{-4})$, $^{18}O(0.205,1.6 \times 10^{-4})$. The values listed in the parentheses represent the % of natural abundance and thermal neutron capture cross section (barn). The capture cross section is the effective cross sectional area of the atom that exposes itself to absorption; this is also a measure of the probability of neutron capture [43,44].

Some of the eight isotopes in ZnO become transmuted by interactions with thermal neutrons with energy $\sim$ 25meV. Fast neutron cross sections for the eight isotopes are insignificant. The relevant nuclear reactions can be found in Table 1, where n,γ,e,ν, and β denote thermal neutron, gamma ray, electron, neutrino and beta ray,

respectively. After the nuclear reactions ^{64}Zn, ^{68}Zn, ^{70}Zn and ^{18}O are transmuted to ^{65}Cu, ^{69}Ga, ^{71}Ga and ^{19}F, respectively. Isotope concentration $C = C_i\, n\, \sigma\, f$, where C_i, n, σ, and f are the constituent atom concentration, natural abundance, capture cross section, and thermal neutron flux, respectively. The calculated concentrations in cm^{-3} of generated isotopes for samples irradiated with neutron flux 1.8×10^{17} n/cm^2 are 2.71×10^{15}, 1.23×10^{15}, 4.11×10^{13}, and 2.41×10^9 for ^{65}Cu, ^{69}Ga, ^{71}Ga and ^{19}F, respectively. The nuclear reactions for the Zn and O isotopes can be found in Table 1 [44].

Table 1. Nuclear reactions for Zn and O isotopes with thermal neutrons.

Isotope	Nuclear Reaction		Half-life	Decay Energy
^{64}Zn	^{64}Zn (n, γ) ^{65}Zn	^{65}Zn →^{65}Cu+γ	244.26 days	1.352 MeV
^{66}Zn	^{66}Zn (n, γ) ^{67}Zn		Stable	-
^{67}Zn	^{67}Zn (n, γ) ^{68}Zn		Stable	-
^{68}Zn	^{68}Zn (n, γ) ^{69}Zn	^{69}Zn →^{69}Ga+ β$^-$	56.4 min	0.438 MeV
^{70}Zn	^{70}Zn (n, γ) ^{71}Zn	^{71}Zn →^{71}Ga+ β$^-$	2.45 min	2.813 MeV
^{16}O	^{16}O (n, γ) ^{17}O		Stable	-
^{17}O	^{17}O (n, γ) ^{18}O		Stable	-
^{18}O	^{18}O (n, γ) ^{19}O	^{19}O →^{19}F+ β$^-$	26.91 sec	4.821 MeV

3.4.1.2 Hall Measurements

Hall measurements of control and irradiated bulk samples showed n-type conduction. Table 2 shows the results of the Hall measurements for the control and dosed samples [43].

Table 2. Hall measurement results for control and irradiated samples.

Dose (cm^{-2})	Sheet resistance (Ω/sq.)	Sheet carrier density (cm^{-2})	Bulk carrier density (cm^{-3})	Mobility (cm^2/Vs)
0	$3x10^3$	$2.8x10^{13}$	$9x10^{14}$	10
$3.6x10^{16}$	$3x10^4$	$9x10^{13}$	$8x10^{14}$	23
$3.6x10^{17}$	93	$1.8x10^{15}$	$3.6x10^{16}$	37
$7.2x10^{17}$	47	$3.2x10^{15}$	$6.4x10^{16}$	43

The properties of the bulk ZnO samples with and without annealing are compared in Figure 31.
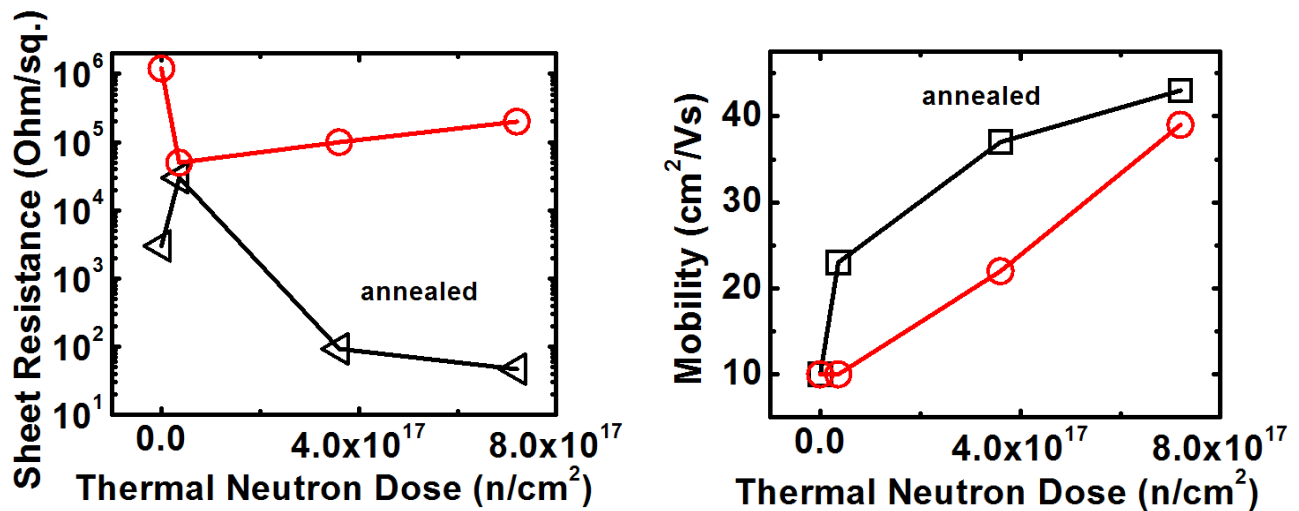
Figure 31. (a) Comparison of sheet resistance in bulk ZnO samples as a function of dose with and without annealing. (b) Mobility determined from Hall measurements as a function of neutron dose and annealing [44].

From the plots we can see that annealing decreased sheet resistance while increasing mobility as well as carrier concentration for all doses. The concentration of

carriers in the control sample increased 200x while the irradiated samples increased 1000x after annealing. Neutron irradiation increased the mobility even in the un-annealed samples. In addition, annealed irradiated samples showed an increase of maximum carrier concentration of about 60x when compared to the unirradiated sample shown in Figure 32. Examining only the annealed sample and the effect of dose on it, it can be seen that the neutron irradiation plays a significant role in the transport properties of ZnO seen in Figure 33.
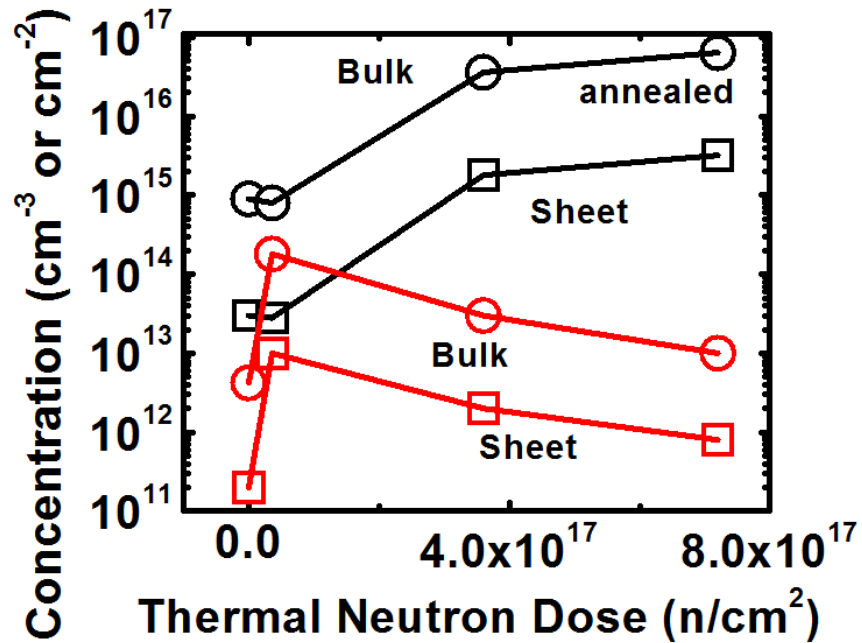
Figure 32. Comparison of surface and bulk carrier concentrations [44].
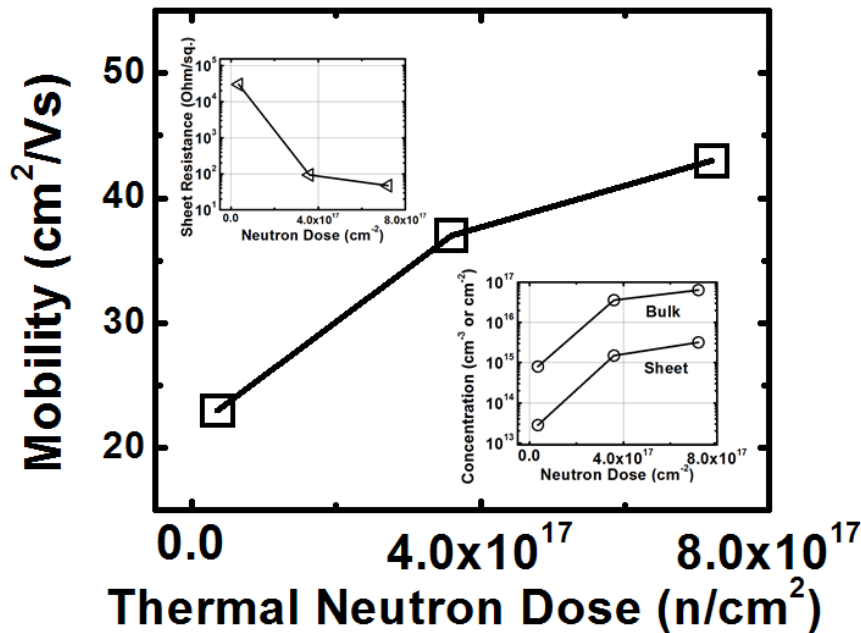
Figure 33. Dependence of electron mobility in ZnO on neutron irradiation dose. Upper insert: sheet resistance dependence on neutron irradiation dose. Lower insert: carrier density dependence on neutron irradiation dose [43].

3.4.1.3 Optical Properties of Bulk

CL spectra are compared for the bulk samples with zero and maximum dose in Figure 34. The spectra displays a near-band-edge (NBE) emission at ~385 nm and a broad band emission centered in the visible range. The intensity of the band-to-band transition is increased while the visible band center shifts from ~500 to 580 nm. While the integrated intensity remains almost unaffected; the emission is redistributed in favor of the NBE transition. The NBE emission includes both conduction-band to neutral-acceptor transitions (e, A^0) and shallow donor-acceptor pair (DAP) recombination. The intensity of the NBE may point to an increase in shallow donor concentration [43].
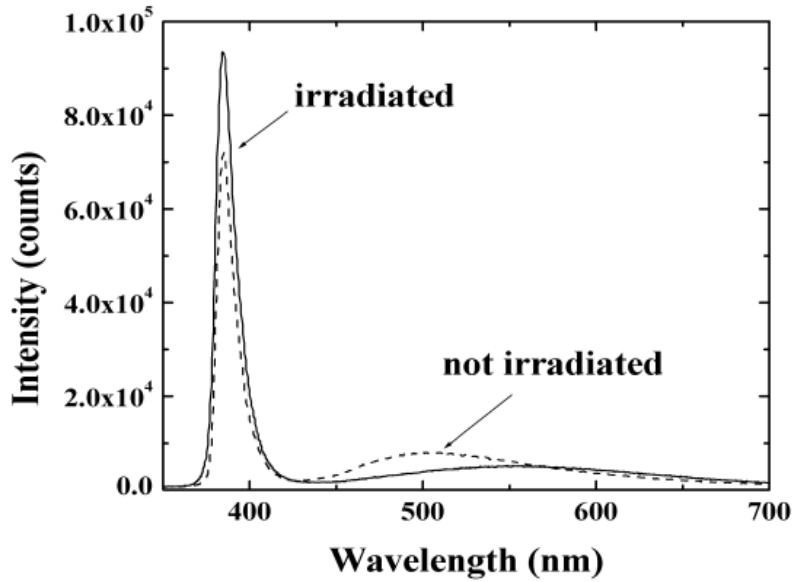
Figure 34. Room temperature CL spectra of bulk sample 1 (dashed line) and bulk sample 4 (solid line) [44].

(a)

(b)
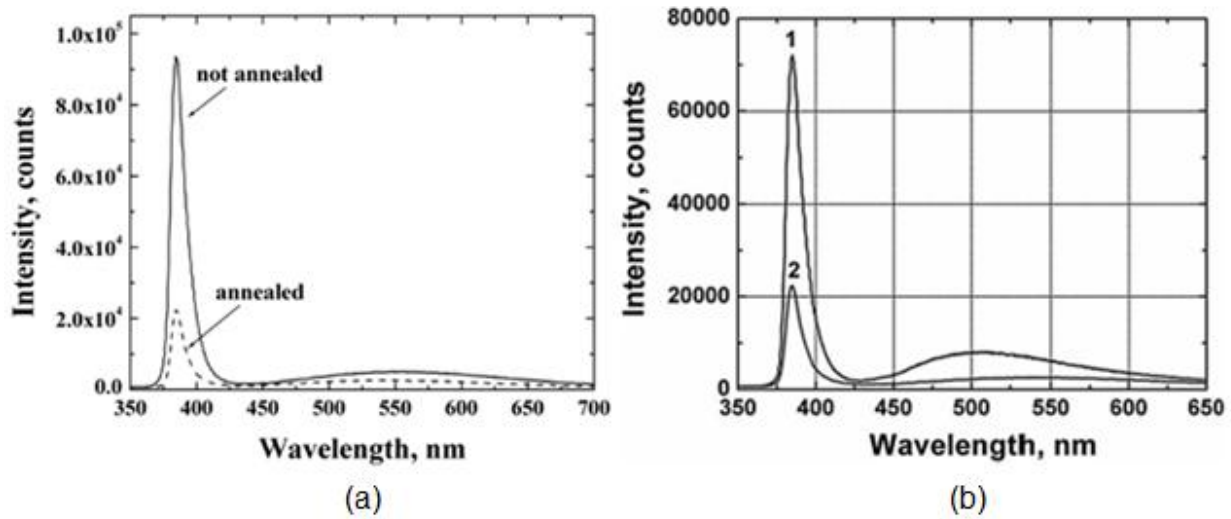
Figure 35. (a) Room temperature CL spectra of sample 4 before (solid line) and after (dashed line) annealing. (b) Room temperature CL spectra taken from control sample (1) and the sample exposed to the maximum dose 7×10^{17} cm^{-2} (2) [44].

The bulk sample subjected to the highest dose was also annealed and the effects on intensity shown in Figure 35(a). The reduction of the peaks indicates an increase of carrier lifetime. The difference in peak intensities in the un-irradiated control sample and the sample with the maximum dose after annealing (2) is shown in Figure 35(b). Neutron irradiation significantly decreases the intensity of the NBE emission when compared with that in the control sample, and shifts the visible band center from ~505 to 550 nm. However, the irradiation does not change the ratio of NBE-to-broad band emission [44].

Neutron irradiation of ZnO displaces zinc atoms into interstitial sites creating neutral point defects, Zn_i^0, which contribute no electrical conductivity yet [64]. As the crystal's temperature is low (under 100-150°C), hole traps in ZnO, in the form of impurities or positive-ion vacancies can stabilize Zn interstitial in the neutral state. Annealing then leads to the thermal ionization of these hole traps. The holes return back to the interstitial Zn_i^0 atoms and form Zn_i^{1+} and Zn_i^{2+} species, which act as shallow donors with an activation energy of ~ 30 meV [65]. Annealing also contributes to the improvement of the material's crystallinity with an increase in carrier (electron) lifetime in the conduction band due to a decrease in scattering. As the lifetime is increased the amount of radiative recombination events that can take place is decreased and thus the intensity of the CL becomes diminished. We can conclude that due to the improvement of lattice crystallinity from annealing and irradiation-induced formation of electrically active species of interstitial Zn we observe the effects illustrated above [43].

3.4.1.4 Optical Properties of Nanostructures

Next, we look at the nano-structured ZnO samples as-grown and irradiate shown below in SEM micrographs in Figure 36. The nanostructured and control bulk samples were irradiated by neutron doses 1.5×10^{14}; 6×10^{14}; 1.5×10^{15} and 6×10^{16} n/cm^2 in the vertical port of the University of Florida Training reactor.
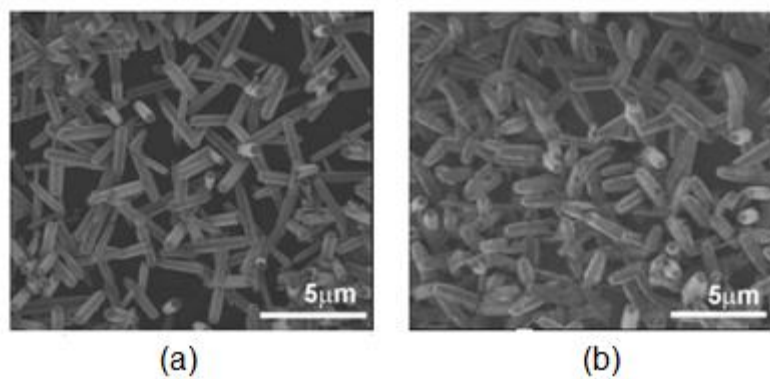
Figure 36. SEM images of ZnO nanocrystals. (a) As grown sample and (b) Irradiated sample [43].

The CL spectra of the ZnO nano-rod based sample displays a strong and sharp UV emission at 385 nm shown in Figure 37. This UV emission corresponds to the near band edge emission of ZnO. The strong peak at 385 nm and weakness of the following broad green emission band indicate that the nanorods must have good crystal quality. A blue shift of the NBE line appears as a result of neutron irradiation as does the appearance of a broad blue-green emission band for both nano- and mono- crystal samples [43].
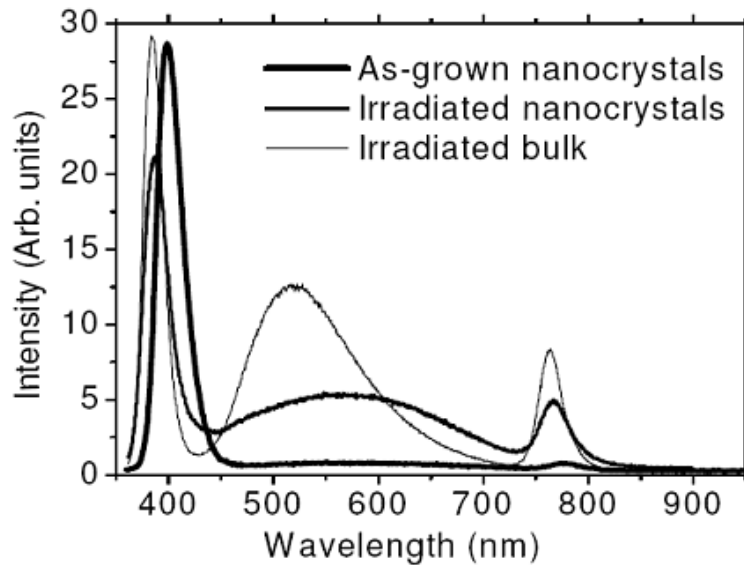
Figure 37. Comparison of CL spectra of ZnO bulk and nano-rod samples for various irradiation conditions [44].

Low energy emission can be from the manifestation of several different contributions such as oxygen vacancies, zinc interstitials and radiation defects [66-68]. Therefore, we use this aspect of the CL spectra as an indicator for radiation hardness. Even though the neutron dose for the bulk sample was more than two orders of magnitude lower than the dose for the nano-crystal sample the radiation-defect band is considerably stronger. This is a clear sign that nanocrystalline ZnO is more radiation hard than the bulk samples. This combined with high optical quality of the ZnO nanorods makes a good case for these structures being developed for optical devices able to operate in radiation harsh environments.

CHAPTER FOUR – DISCUSSION

In this research we begin with a p-n ZnO homojunction and a temperature induced increase in L seen in the p-type Sb doped ZnO region. This increase may be attributed to the growing lifetime of nonequilibrium minority carriers. A thermal activation energy of 145±10 meV was calculated by measuring the diffusion length at various temperatures [42]. This activation energy may represent carrier delocalization energy and serves as a parameter for determining the increase of the diffusion length due to the reduction in recombination. Previous CL studies on ZnO:Sb epitaxial layers suggest that the recombination route of nonequilibrium carriers emerge from transitions to a deep, neutral acceptor level (e,A^0) [54,56]. When the sample is exposed to an increase in temperature the fraction of acceptors that are ionized are also increased. This is turn reduces the concentration of A^0 which hinders the recombination rate. Equation 1.2 shows the diffusion length, L, in correlation with the diffusion coefficient, D, and lifetime, τ. Therefore, as the recombination rate decreases, the lifetime of the minority electrons in the conduction band increases, leading to an increase in L.

From there we precede to electron injection of p-type Sb doped ZnO nanowires. Here we get similar temperature induced increase in L which is related to the temperature induced increase seen in the previous sample due to reduction in recombination efficiency. Electron irradiation was shown to also produce an increase L but with a corresponding reduction in rate with increasing temperature.

The effect of electron irradiation on the diffusion length is attributed to the trapping of non-equilibrium electrons on the neutral acceptor levels ($A^0+e^-{\rightarrow}A^-$). When the non-equilibrium electron-hole pairs recombine, they involve the levels of neutral acceptors located deep in the band gap. Electron trapping on neutral acceptor levels prohibits the pathway of recombination via these levels and leads to an increase of non-equilibrium minority carrier (electron) lifetime in the conduction band and, in turn, carrier diffusion length. As the excitation continues, the concentration of neutral levels decreases, due to electron trapping on them, while the diffusion length steadily rises. With the thermal activation energy of 112±3 meV we found an activation energy for the electron effect to be 233±10 meV.

The same sample was then measured using Cathodoluminescence measurements. With an increase in temperature we see a decrease in intensity. When an activation energy is found for the effect, 115±10 meV, it is similar to the activation energy of the increase seen in EBIC measurements of *L*. We also test the effects of electron irradiation on this sample and find that the intensity also decreases with increased duration of exposure with a corresponding decrease in rate due to temperature. This activation energy was found to be 212±15 meV which is in agreement with the activation energy found as a result of electron irradiation induced increase of *L*. This suggests that the same process is responsible for both the increase in *L* and the decrease in CL intensity and that the intensity of the CL NBE spectra directly correlates with carrier lifetime. The lower the intensity of the CL NBE spectra peak the longer the minority carrier lifetime and subsequently the longer the minority carrier diffusion length.

In another p-type Sb doped ZnO nanowires we investigated the effects of forward bias electron injection and temperature. This sampled displayed a similar increase in L with temperature and forward bias electron injection that the electron irradiated sample had shown and that it comes from a similar origin to that of the electron beam irradiation-induced increase. Since the presence of Sb has been shown to induce acceptor levels in the band gap far from the valence band edge, it is likely that application of a forward bias would result in similar effects. This is due to the electrons being injected into p-ZnO becoming trapped on the Sb-related levels preventing further recombination via these levels and subsequently resulting in the increase of L. With the thermal activation energy of 144±5 meV we found an activation energy for the electron effect to be 217±20 meV, similar to the activation energies found for electron irradiated ZnO nanowires [41].

It has been theorized by Limpijumnong et al. that the role of acceptors in size-mismatched Sb-impurity doped ZnO is accomplished by a Sb_{Zn}-$2V_{Zn}$ complex, which is predicted to have an ionization energy of 160meV [20]. While our value for activation energy (217-233 meV) is somewhat larger than the predicted value (160 meV), we can successfully rule out other Sb-related defects such as Sb_o substitutional defects as well as the single vacancy Sb_{Zn}–V_{Zn} complex, due to their ionization energies being about an order of magnitude larger than our value [20]. It has also been shown that in Sb-doped ZnO, acceptor activation energy can vary from about 135 meV (1.3×10^{18} cm^{-3}) to 212 meV (1.3×10^{17} cm^{-3}) depending on its concentration of majority carriers [11]. This increase in L by electron injection is not seen in n-type ZnO.

From our investigation of impurity activity in p-type ZnO samples, we move on to impurity activity in n-type ZnO. Only a slight temperature induced increase in L and an insignificant electron irradiation increase in L is shown experimentally. This helps to confirm our theorized role of acceptors in the p-type ZnO samples. However, CL measurements can be used to infer impurity activity in n-type ZnO, since a dependence can be seen in CL intensity with temperature and electron irradiation. As electron irradiation duration increases a decrease in the CL intensity can be seen. This is due to an increase of electron lifetime in the conduction band. As temperature is increased a decrease in rate of CL intensity decrease is also seen. This rate decrease suggests that a thermally activated process, counter to the lifetime increase, induced by electron injection, exists simultaneously. This process can be described by trapped electrons overcoming an energy barrier (since this process is activated by an increase in temperature) and recombining with the holes in the valence band. Then when the temperature is raised, more trapped electrons overcome the barrier, thus reestablishing the recombination pathway and slowing the increase of the electron lifetime. The activation energy obtained for this sample was 259±30 meV. This energy is in reasonable agreement with interstitial Zn (Zn_i) localization in the ZnO forbidden gap – 290meV [40]. From this we can conclude that interstitial zinc is the best candidate responsible for the observed effect.

We now have an idea of how impurity activity influences both n and p–type ZnO samples through thermal and electron injection. We move on to how neutron irradiation effects the transport properties of n-type ZnO nanostructures. We studied bulk mono

and nanocrystal ZnO samples exposed to various amounts of neutron irradiation. We found that changed can be seen in the CL spectra of the neutron irradiated samples. When a bulk sample is exposed to irradiation it produces an increase in its NBE peak when compared to a nonirradiated sample. This increase may indicate an increase in concentration of shallow donors. When this sample is then annealed, the CL intensity is diminished much greater than the nonirradiated intensity. As seen before, this corresponds to an increase in carrier lifetime. The irradiated and annealed sample also shows a doubling of mobility values. This is due to the effects of neutron irradiation on the zinc atoms. When irradiated by neutrons the displaced zinc atoms create neutral point defects, Zn_i^0. Hole traps stabilize Zn interstitial atoms in the neutral state at low temperature. Once annealed these hole traps become ionized and return back to the interstitial Zn_i^0 atoms and form Zn_i^{1+} and Zn_i^{2+} species, which act as shallow donors. Annealing also contributes to the improvement of the material's crystallinity with an increase in carrier (electron) lifetime in the conduction band due to a decrease in scattering [43,44].

Then we expose the nano-structured ZnO samples to neutron irradiation. Low energy emission can be associated to oxygen vacancies, zinc interstitials and radiation defects. When the nano-structured ZnO samples are compared by CL spectra to irradiated bulk, we see a smaller low energy defect band than in the bulk. We can conclude from this that the nano-structured ZnO samples are more radiation hard than the bulk [44].

CHAPTER FIVE – CONCLUSION

5.1 Thermal effects on minority carrier diffusion length and lifetime in ZnO

For p-type ZnO doped with Sb, the minority carrier diffusion length was seen to increase while the CL intensity of the NBE transition was seen to decrease when exposed to increasing temperature. This dependence led to the extraction of activation energies which were in good agreement with each other and suggest that both observations are due to the same process. The capture cross section is inversely proportional to temperature which reduces the recombination rate as the temperature increases. This was seen in both bulk ZnO and nanorod ZnO material.

5.2 Electron injection effects on minority carrier diffusion length and lifetime in ZnO

When exposed to continuous electron irradiation the samples p-type ZnO doped with Sb showed an increase in minority carrier diffusion length as well as a corresponding decrease in CL intensity of the NBE transition with increased duration of exposure. This was found to be due to the trapping of non-equilibrium carriers on non-ionized acceptor levels. Recombination cannot proceed once this occurs and leading to an increase in minority carrier lifetime and diffusion length. A conflicting process which slowed the rate of electron irradiated induced growth in minority carrier diffusion length as well as the rate of decrease in CL intensity, emerged as temperatures increased.

This is what occurs when the recombination pathway becomes restored by the trapped electron gaining enough thermal energy to escape.

From these temperature dependent EBIC and CL measurements under continuous electron excitation we are able to obtain activation energies for the irradiation induced changes. These values for the activation energy of the electron irradiation induced effect found in p-type ZnO doped with Sb are consistent with the ionization energy of the Sb_{Zn}-$2V_{Zn}$ acceptor complex.

In n-type ZnO, CL intensity of the NBE transition was shown to decrease with temperature and electron irradiation with a similar counteracting process with increasing temperature seen in p-type ZnO material. The activation energy for the electron irradiation induced effect found in n-type ZnO through CL observation was found to be in reasonable agreement with that of interstitial Zn localized in the ZnO forbidden gap.

Activation energies due to thermal and electron irradiation effects of the ZnO samples are presented in Table 3.

Table 3. Material with thermal and electron injected activation energies.

Sample Material	Measurements	ΔE_a (meV) Thermal	ΔE_a (meV) Electron Injected	Defect Ionization energy (meV)
P-type Sb doped on n-type Ga-doped ZnO on Si substrate	EBIC	145±10	X	Sb_{Zn}-$2V_{Zn}$ E_a=135-212
P-type Sb doped nanowires on n-type ZnO on Si substrate	EBIC	112±3	233±10	Sb_{Zn}-$2V_{Zn}$ E_a=135-212
	CL	115±10	212±15	Sb_{Zn}-$2V_{Zn}$ E_a=135-212
P-type Sb doped on n-type ZnO on Sapphire substrate	EBIC	144±5	217±20	Sb_{Zn}-$2V_{Zn}$ E_a=135-212
N-type ZnO on Si substrate	CL	X	259±30	Zinc Interstitial E_a=290

5.3 Neutron irradiation effects on minority/majority carrier diffusion length and lifetime in ZnO

When N-type ZnO crystals were exposed to neutron irradiation the ZnO luminescence spectrum was seen to change. Based on these observations we were able to conclude that exposure to neutron irradiation increases majority carrier lifetime with dose and annealing. Hall measurements also confirmed the overall enhancement of n-type conductivity. This is believed to be due to the formation of electrically active Zn_i with crystal lattice improvements from annealing. CL observations of both bulk and nanorod ZnO proved the superior radiation hardness of the ZnO nanorods. This is likely

due to the much higher specific surface area which facilitates migration of the radiation defects towards the surface. This may also be attributed to the stopping depth of the neutrons in the nanostructures.

APPENDIX A – RELATED WORKS IN PROGRESS

This section contains work which is related to the research conducted in chapter three that are currently being analyzed. Since there is no concrete conclusion to these experiments, only the preliminary results and theories will be presented.

A.1 Neutron irradiation of p-type ZnO nanowires doped with Sb

Sb doped, p-type nanowires which were irradiated with neutrons were studied. The sample was grown using a thermal scientific quartz tube on a silicon substrate by plasma assisted molecular beam epiatxy. Part of the ZnO film and nanowires were covered with an Ag contact. A similarly grown sample was used for the forward bias electron injection of the ZnO nanowires described previously. Temperature dependent EBIC and CL measurements were conducted on the sample.

A.1.1 Minority carrier transport properties

The EBIC signal was recorded within the p-type nanowire layer, beginning from the n-ZnO/p-ZnO interface, on a sample cleaved perpendicular to the plane of growth. In Figure 38, one can see the superimposed EBIC line-scan signal following a path of exponential decay versus beam-to-barrier distance in the p-type ZnO nanowire region. All experiments were conducted *in-situ* in a Philips XL30 Scanning Electron Microscope (SEM) under an accelerating voltage of 20kV.
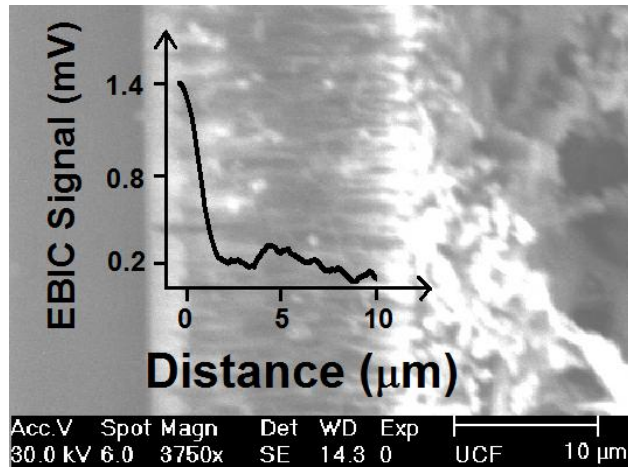
Figure 38. Secondary electron image of the sample cross-section taken perpendicular to the growth plane. Going left to right: silicon substrate, epitaxial n-ZnO, p-ZnO nanowires, and the Ag contact. EBIC line scan superimposed.

Temperature dependent diffusion length measurements were taken at temperatures ranging from 25 to 125°C by EBIC line scans of 24 seconds. New locations for the scan were chosen for each temperature.
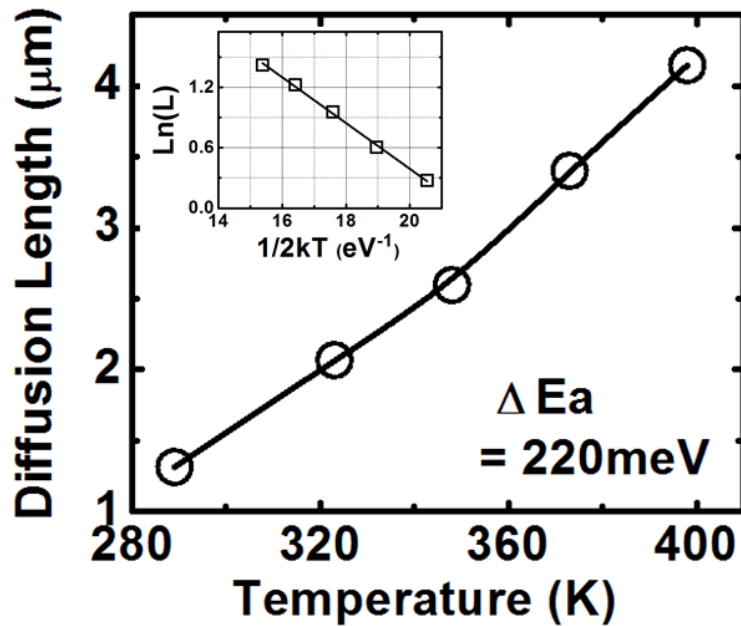
Figure 39. The diffusion length as a function of temperature. Insert: Arrhenius plot for *Ln(L)* vs. 1/2*k*T dependence resulting in the activation energy of 220±10 meV.

As the temperature was raised in the sample the diffusion length was seen to become increased. The relationship between diffusion length, *L*, and temperature is shown in Figure 39. The value of *L* increases exponentially with temperature increase; this is fitted to Equation 2.4. The thermal activation energy was found from the Arrhenius plot to be 220±10 meV. This energy likely represents carrier delocalization energy and determines the increase of the diffusion length due to the reduction in recombination efficiency [41].

A.1.2 Optical Properties

CL measurements were conducted in-situ in a Philips XL30 Scanning Electron Microscope (SEM), integrated with a Gatan MonoCL3 CL system. Using CL measurements we obtain spectra ranging from wavelengths 350 nm to 850 nm with a peak ranging from 384 nm to 391 nm. This peak intensity was collected and average against varying temperatures from 25^oC to 125^oC. All measurements were taken using a 20kV electron beam voltage and at a magnification of 12800x. For each temperature a new area was selected.
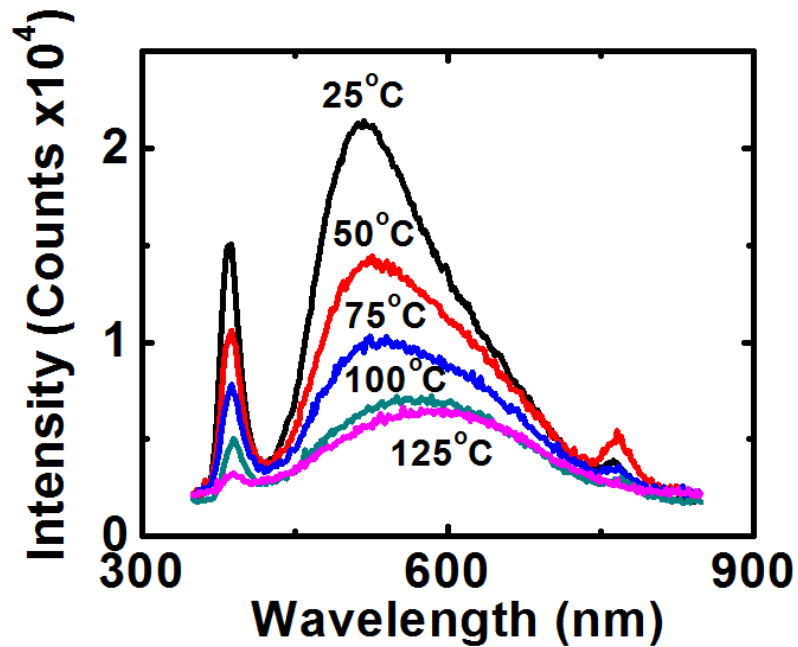
Figure 40. CL spectra Intensity vs. wavelength for temperatures 25^oC to 125^oC.

Figure 40 shows the decay of the intensity of the NBE due to temperature increase. It also shows a strong low energy defect band located from about wavelength 450 nm to 700 nm [43,44].

Using Equation 2.5 to define the relationship between the CL peaks and temperature we can extract the activation energy by plotting Intensity vs. kT as shown in Figure 41. The activation energy was determined to be 235±20 meV.
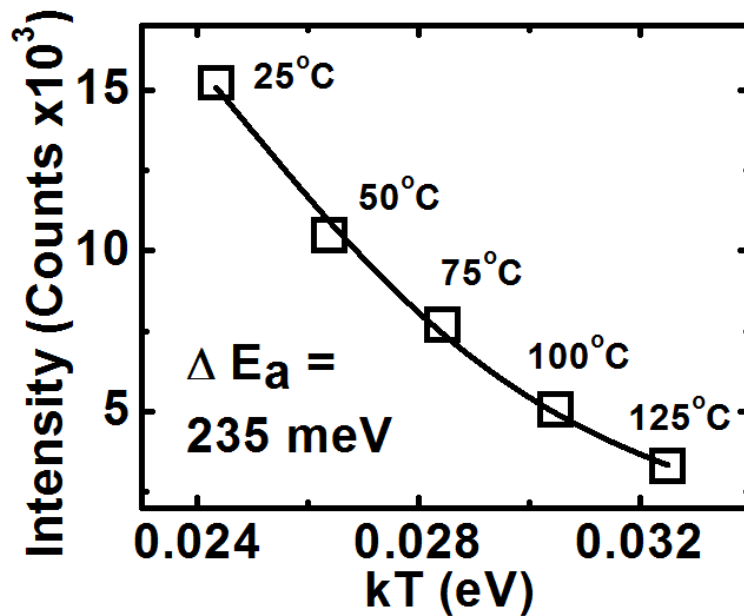
Figure 41. CL spectra Intensity vs. kT for temperatures 25°C to 125°C. An activation energy of ~ 235±20 meV is found.

The thermal activation energy of 235±20 meV is similar to that of the temperature dependent EBIC measurements, 220±10 meV, which suggest that a similar process is responsible for both the increase in diffusion length and the decay of CL intensity as seen before. When non-equilibrium electron-hole pairs are generated by the electron beam they will eventually recombine with each other. Since the hole capture cross-section is inversely proportional to temperature [60,62], the frequency of the recombination events, represented by CL intensity here, decreases with temperature. However, in this case, the thermal activation energy of ~ (220±10 meV to 235±20 meV) is much higher than that found for the similar non-irradiated ZnO nanorod sample (144±5 meV) studied previously [41]. This may be due to the neutron irradiation induced defects in the sample.

A.2 Temperature Dependence of AlGaN/GaN HEMT Devices

Experiments were conducted on eight AlGaN/GaN HEMT devices with an AlGaN layer on top of a GaN layer grown on a sapphire substrate as seen in Figure 42(a). One device was left as a control while the other seven were subjected to degrees of degradation. Temperature dependent EBIC and CL observations were conducted on the samples after the degradation in order to detect any possible changes in transport properties.

A.2.1 Minority Carrier Transport Properties

EBIC measurements were taken between the gate and the drain of each sample as shown in Figure 42(b). Non-equilibrium carriers are generated in semiconductors when exposed to an electron beam of a scanning electron microscope (SEM). As the beam is moved away from the junction in a line scan mode, the current decays as less minority carriers are able to diffuse to the space-charge region. For these samples, line scans of 24 seconds each were collected between the gate and the drain of the middle channels indicated in Figure 42. All experiments were conducted *in-situ* in a Philips XL30 Scanning Electron Microscope (SEM) under an accelerating voltage of 20kV.
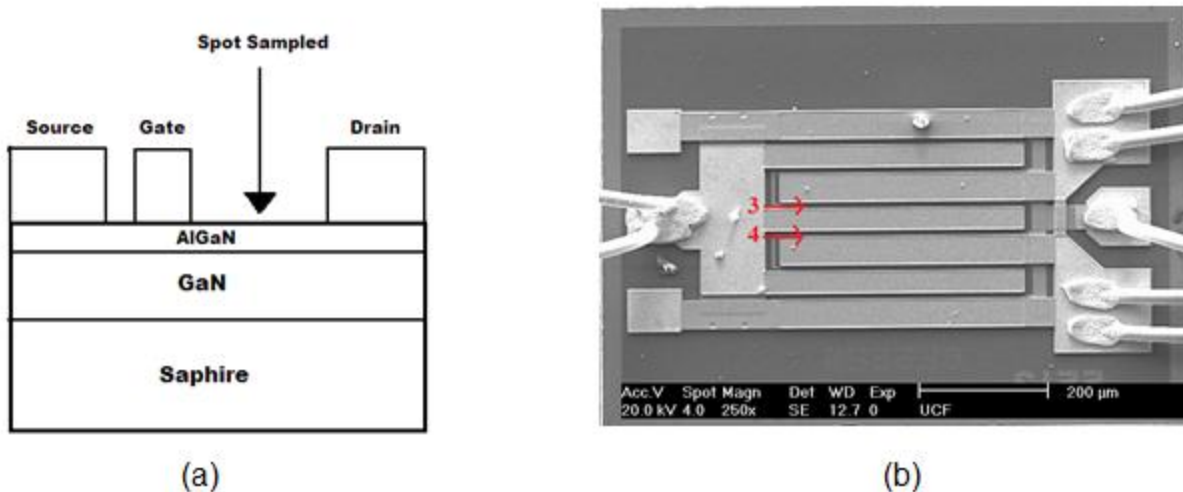
Figure 42. (a) Device viewed height wise. (b) SEM image of device with areas of measurements indicated.

Temperature dependent EBIC measurements were conducted *in situ* in a Phillips XL30 SEM with a hot stage and an external temperature controller (Gatan) for temperature ranging from 25°C to 125°C. Line scans were conducted at different locations for each temperature to avoid unintentional influences of the electron beam.
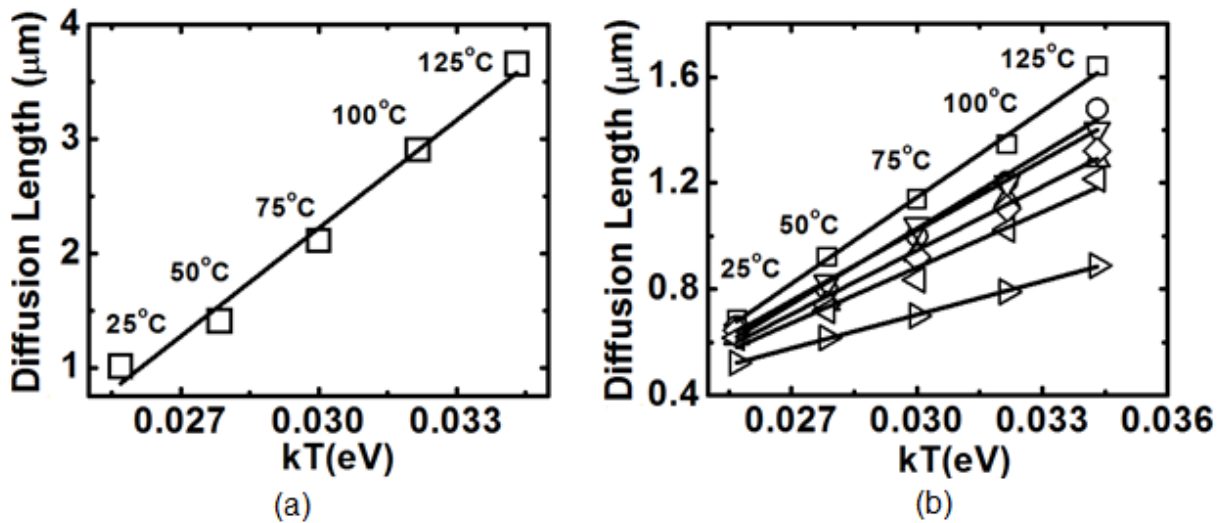
Figure 43. (a) Diffusion length as a function of temperature for the virgin device. (b) Diffusion length as a function of temperature for the seven degraded devices. Device 3573 (squares), device 5618 (circles), device 8512 (down triangle), device 3512 (triangle), device 2273 (diamond), device 9214 (left triangle) and device 5373 (right triangle).

Figure 43 shows that the diffusion length increased with increasing temperature for all samples. We can also see that the diffusion length increased much higher for the virgin sample in Figure 43(a), than for the degraded samples shown in Figure 43(b). Thermal activation energies were calculated using Equation 2.4.
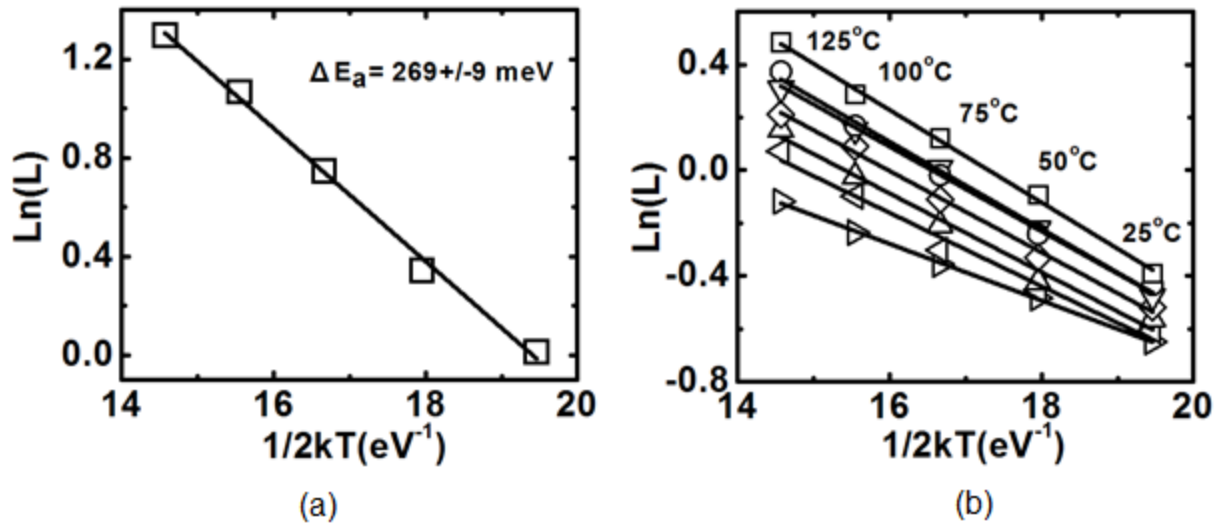
Figure 44. (a) Arrhenius plot of *Ln(L)* vs. 1/2kT yielding a virgin activation energy of 269±9 meV. (b) Arrhenius plot of *Ln(L)* vs. 1/2kT for the seven degraded devices vertically offset for clarity. Activation energies for each device are; Device 3573 (squares) is 175±6 meV, device 5618 (circles) is 165±8 meV, device 8512 (down triangle) is 160±5 meV, device 3512 (triangle) is 154±10 meV, device 2273 (diamond) is 149±12 meV, device 9214 (left triangle) is 139±11 meV and device 5373 (right triangle) is 107±3 meV.

Figure 44 shows the relationship used to extract each sample's activation energy. The thermal activation energy, E_a is said to represent carrier delocalization energy and as a parameter for determining the increase of the diffusion length due to the reduction in recombination.

A.2.2 Optical Properties

CL measurements were conducted in-situ in a Philips XL30 Scanning Electron Microscope (SEM), integrated with a Gatan MonoCL3 CL system and carried out in the same area and channels, as the EBIC measurements, seen in Figure 42(b). Areas of

measurement between the gate and the drain of all AlGaN/GaN HEMT devices, with and without the Field Plate, are shown in Figure 45. Having chosen a collection spot directly between the gate and the drain and then obtaining CL spectral information, we were able to identify the device material and make preparations for optimal data collection. The material displayed strong characteristic GaN spectra at electron beam voltages ranging from 7kV to 20kV, peaking in intensity at 20kV. However, when reducing the beam voltage below 7kV in order to reduce penetration levels to only the surface AlGaN, a characteristic spectra was not obtained. It was concluded that the AlGaN layer was not exhibiting any measurable amount spectra and was therefore not concentrated on during our later testing.
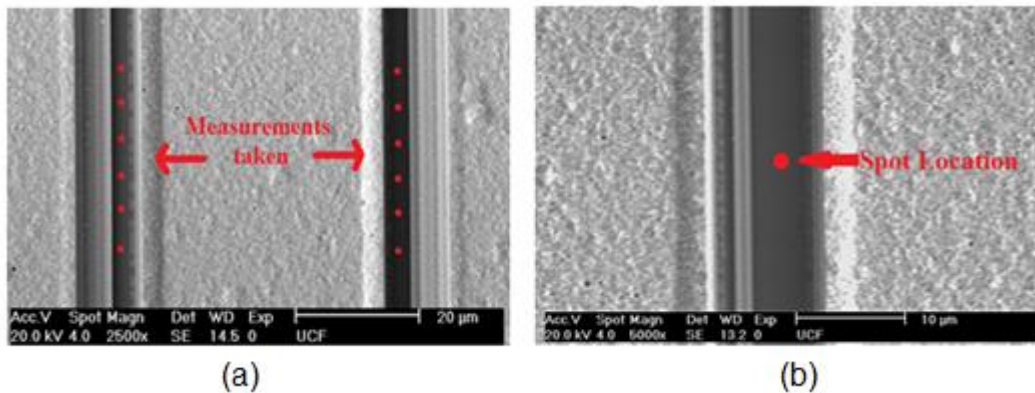
Figure 45. (a) SEM image indicating where CL measurements were made on device with cover over gate. (b) SEM image indicating where CL measurements were made on device with our cover over gate.

Temperature dependent changes in carrier lifetime were analyzed by collecting CL spectra in the near-band-edge (NBE) region. The temperature was varied from $25^{o}C$

to 125°C and the CL spectra collection was conducted in situ in a Phillips XL30 SEM with a hot stage and an external temperature controller (Gatan). Along with the SEM, a Gatan MonoCL3 system allows temperature and wavelength-dependent experiments to be conducted. The peak intensity of the NBE luminescence was recorded at six different spots and averaged in order to evaluate carrier lifetime dependence on temperature. They were taken over wavelengths ranging from 340 nm to 400 nm.
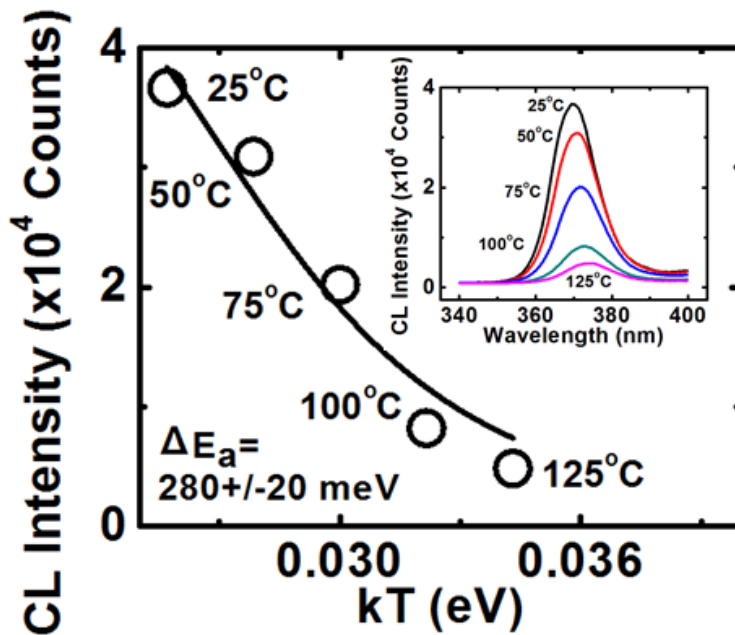
Figure 46. Peak NBE CL spectra intensity of the virgin sample fitted to Equation 2.5 with an activation energy of 280±20 meV. Insert: CL spectra of same device as a function of temperature.

From the insert in Figure 46 you can see a decrease in peak intensity as a function of temperature indicating an increase of carrier lifetime as a result of

decreasing recombination events. This decay can be modeled using the CL Equation 2.5. This is done for all samples and plotted in Figure 47 along with their respective activation energies.
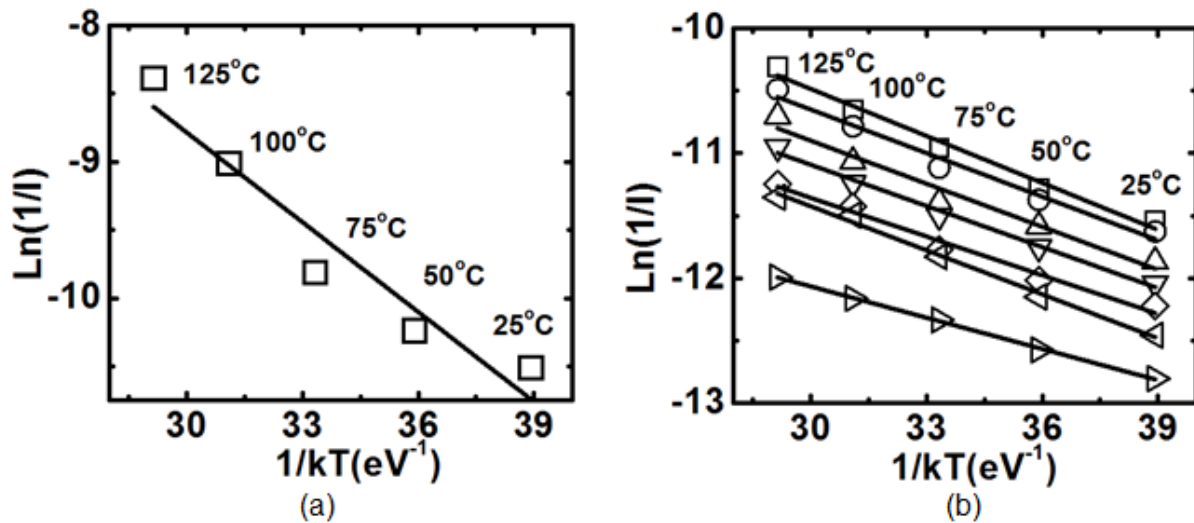
Figure 47. (a) Arrhenius plot for the virgin device CL peak intensity vs kT with an extracted activation energy of 280±20 meV. (b) Arrhenius plot for the seven degraded samples vertically offset for clarity showing the decay of the CL intensity with increasing temperature. Activation energies for each device are; Device 3573 (squares) is 180±10 meV, device 5618 (circles) is 166±10 meV, device 8512 (down triangle) is 155±13 meV, device 3512 (triangle) is 160±22 meV, device 2273 (diamond) is 150±10 meV, device 9214 (left triangle) is 147±19 meV and device 5373 (right triangle) is 103±13 meV.

The activation energies for all devices including both EBIC and CL observations are listed in Table 4 along with their corresponding test time and degradation. In Figure 48 we can then establish a correlation between time of test and diffusion length and activation energy.

Table 4. Activation energies and degradation for all devices.

Device	Degradation	EBIC E_a	CL E_a
Virgin	0	269±9 meV	280±20 meV
5373	Step stress @CW: Tch~215;20h;no degradation Tch~240;30h;no degradation Tch~265;24h;no degradation Tch~290;70h;0.7 dB	107±3 meV	103±13 meV
3573	Tch 288C,CW,89h,0.82 dB	175±6 meV	180±10 meV
5618 (FP)	Tch 290C, CW,7.9h,1dB	165±8 meV	166±10 meV
3512 (FP)	Tch 275C, CW, 35.2h,1 dB	154±10 meV	160±22 meV
8512 (FP)	Tch 275C, CW, 7h,1 dB	160±5 meV	155±13 meV
2273	Tch 281C, CW,75h,1 dB	149±12 meV	150±10 meV
9214 (FP)	Tch 250C, CW,1.5h, system failure	139±11 meV	147±19 meV

*FP is field-plate
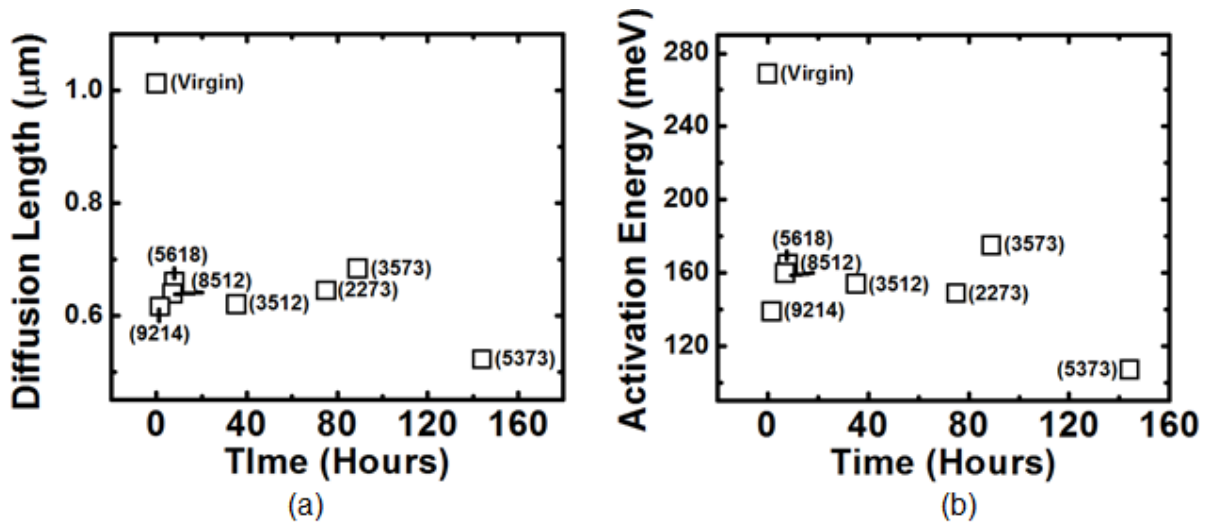
Figure 48. (a) Diffusion length of each device at room temperature vs. duration of test. (b) EBIC thermal activation energy for each device vs. duration of test.
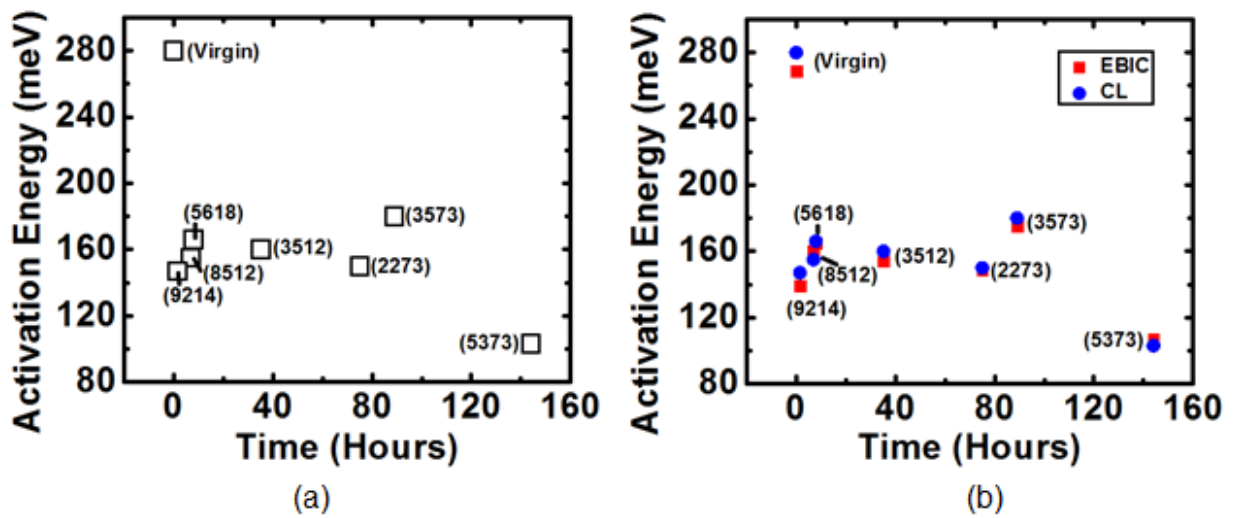
Figure 49. (a) Thermal activation energies for each device based on CL peak intensity vs. duration of test. (b) Activation energies for both EBIC (red squares) and CL (blue circles) measurements vs. duration of test.

All samples exhibited a thermal dependence. When observed though EBIC measurements of minority carrier diffusion length, L, was shown to increase with temperature. When observed by CL measurements, the intensity was shown to decrease with temperature as seen in Figure 49(a). EBIC measurements correlate nicely with the CL measurements for each device shown in Figure 49(b). The experiments have demonstrated that the activation energies for devices after degradation are consistently lower than that with no test (virgin device). Overall diffusion length and thermal activation energies for EBIC and CL measurements were seen to decrease with duration of device test.

Amount of degradation may also be linked to activation energy with the virgin device having the highest activation energy (269-280 meV) and no degradation. The device that suffered 0.82 dB degradation has the next highest activation energy of (175-180 meV). Devices that had 1 dB degradation (5618,3512,8512,2273) all have activation energies between (149-166 meV). Outliers include, device 9214, which had a system failure and had a lower activation energy of (139-147 meV). Also, device 5373 had a lower degradation but was exposed to a longer test and showed the lowest activation energy at (103-107 meV). Devices with a field plate deviated less in their activation energies.

Degradation of the device leads to a certain involvement of a mechanism of defects and trapping indicated by the decrease in activation energy values [69].

A.3 Proton Irradiation of InAlN/GaN HEMT Devices

The InAlN/GaN devices were grown with a MOCVD system beginning with a thin AlGaN nucleation layer, followed by a 1.9 µm low-defect carbon-doped GaN buffer layer, 50 nm undoped GaN layer, 10.2 nm undoped InAlN layer with a 17% of In mole fraction, and capped with a 2.5 nm undoped GaN layer. This was all grown on a *c*-plane sapphire substrate measuring three inches in diameter. Sheet carrier densities of the as grown structures measured 2.1×10^{13} cm^{-2} with an electron mobility of 1000 cm^2/V-s [70,71].

Proton irradiations were performed using a MC 50 (Scanditronix) cyclotron located at the Korea Institute of Radiological & Medical Sciences (KIRAMS). The proton energy at the exit of the cyclotron was 30 MeV and the proton energy at the sample was decreased to 5 MeV after protons passed through aluminum degraders. Each aluminum degrader was measured to have a thickness of 2.7 mm. The entire beam current was measured using Faraday-cup to calculate flux density. Samples were dosed with 2×10^{11}, 2×10^{13}, and 2×10^{15} protons/cm^2. The stopping depth of 5 MeV protons in the InAlN/GaN substrate was more than 100 µm, estimated with the TRIM program [70,71].

A.3.1 Minority Carrier Transport Properties

Electron Beam Induced Current (EBIC) measurements were conducted on InAIN/GaN High Electron Mobility Transistors samples seen in Figure 50(a). Experiments were done *in-situ* in a SEM and under the electron beam accelerating voltage of 20kV. Measurements were taken between the gate and the drain, indicated in Figure 50(b), at a magnification of 25000x. The first sample was the reference sample, then the samples dosed with $2x10^{11}$ cm^{-2}, $2x10^{13}$ cm^{-2} and $2x10^{15}$ cm^{-2} were tested. A diffusion length was calculated from the EBIC measurements seen for one measurement in Figure 51, for each sample at temperatures varying from 25°C to 125°C.

(a) (b)
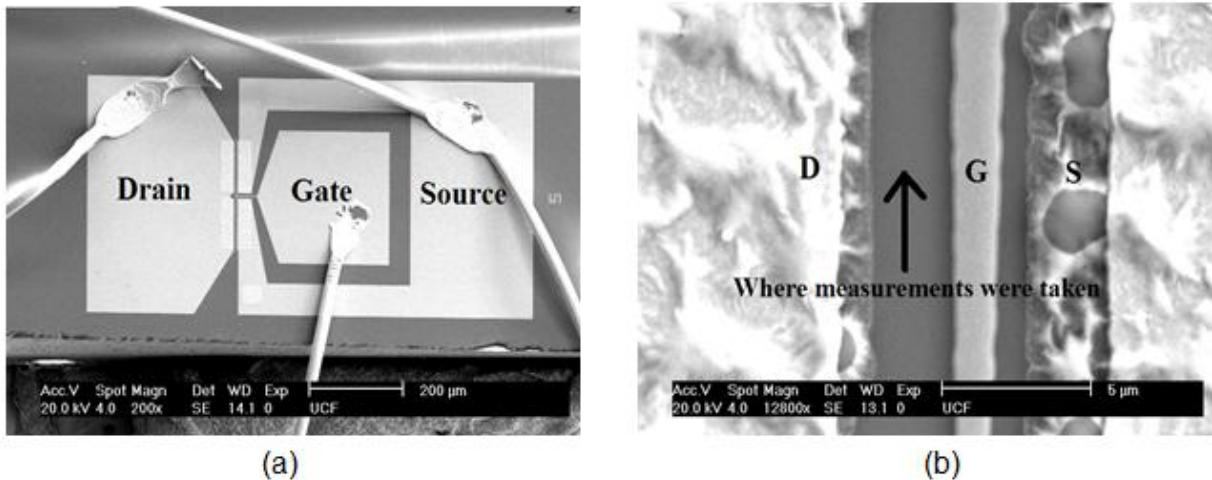
Figure 50. (a) SEM Image of entire device. (b) SEM Image indicating where the measurements were taken [71].
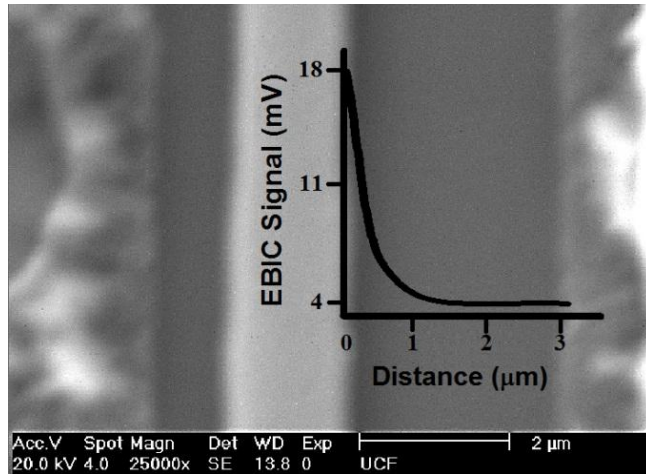
Figure 51. SEM Image with superimposed EBIC signal vs distance [71].
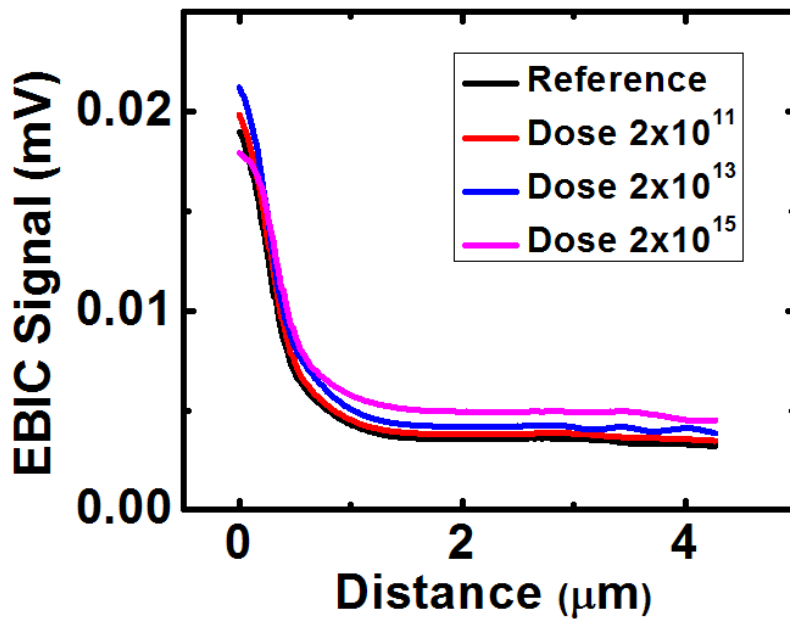
Figure 52. EBIC signal vs distance for reference and all three proton doses [71].

Table 5. Calculated values of the diffusion lengths for the 4 samples all at 25°C [71].

Sample	Average Diffusion Length Value (µm)	Standard Deviation
Reference	0.982253	0.00938331
Dose 2x10^{11} cm^{-2}	1.02543	0.0575009
Dose 2x10^{13} cm^{-2}	1.07053	0.0468171
Dose 2x10^{15} cm^{-2}	1.09431	0.0334550

The minority carrier diffusion length was found to be about 1 µm independent of proton dose as seen in Figure 52. Very little difference was found in the diffusion length values when comparing the reference sample to the dosed samples as seen in Table 5. InAlN/GaN HEMTs display high resistance to high energy proton-induced degradation which infers that these devices are very promising for terrestrial and space applications.

A.4 Summary of Related Work

In p-type neutron irradiated ZnO nanowires a thermal activation energy of 235±20 meV and 220±10 meV resulted from temperature dependent CL and EBIC measurements. This was found to be much higher than the thermal activation energies found in similar samples that were not exposed to neutron irradiation.

Thermal activation energies resulting from an increase in L for AlGaN/GaN devices were also examined. Activation energies found in virgin devices, from EBIC and

CL observations, ranged from 269±9 meV to 280±20 meV. In test degraded devices activation energies were found to be diminished and ranged from 180±10 meV to 103±13 meV.

Proton irradiated InAlN/GaN devices maintained a diffusion length of 1µm independent of proton dose when undergoing EBIC analysis. This indicates a good degree of radiation hardness.

APPENDIX B – BODY OF WORK

B.1 Book Chapter

1. C. Schwarz, L. Chernyak and E. Flitsiyan, "Cathodoluminescence Studies of Electron Injection Effects in Wide-Band-Gap Semiconductors", edited by N. Yamamoto, Cathodoluminescence (2012).

B.2 Articles

1. C. F. Lo, L. Liu, T.S. Kang, H.-Y. Kim, C. Schwarz, E. Flitsiyan, L. Chernyak et al, "Degradation of dc characteristics of InAIN/GaN high electron mobility transistors by 5 MeV proton irradiation" J. Vac. Sci. Technol. B 30, 031202-1 (2012).

2. C. Schwarz, E. Flitsiyan, L. Chernyak, V. Casian, R. Schneck, Z. Dashevsky, S. Chu, J.L. Liu, "Impact of forward bias injection on minority carrier transport in p-type ZnO nanowires" Appl. Phys. Lett. **110**. 056108 (2011).

3. C. Schwarz, L. Yuging, M. Shathkin, E. Flitsiyan and L. Chernyak, "Cathodoluminescence studies of Electron Irradiation Effects in n-type ZnO" J. Phys.: Condens. Matter **23** 334204 (2011).

4. E.S. Flitsiyan, C. Schwarz, L. Chernyak, R.E. Peale, Z. Dashevsky, W.G. Vernetson, "Neutron Irradiation-Induced Enhancement of Electronic Carrier Transport in ZnO" "Radiation Effects & Defects in Solids" Vol.166, No.2, **104-108** (2010).

5. L. Chernyak, C. Schwarz, E.S. Flitsiyan, S. Chu, J.L. Liu, K. Gartsman, "Electron beam induced current profiling of ZnO p-n homojunctions". Appl. Phys. Lett. **92**. 102106 (2008).

6. E.S. Flitsiyan, C. Schwarz, R.E. Peale, O. Lupan, L. Chernyak, L. Chow, W.G. Vernetson, Z. Dashevsky, "Neutron Transmutation Doping and Radiation Hardness for Solution-Grown Bulk and Nano-Structured ZnO" Mater. Res. Soc. Symp. Proc. Vol. **1108** (2008).

B.3 Conferences and Poster Presentations

7. E.S. Flitsiyan, C. Schwarz, R.E. Peale, O. Lupan, L. Chernyak, L. Chow, W.G. Vernetson, Z. Dashevsky, "Neutron Transmutation Doping and Radiation Hardness for Solution-Grown Bulk and Nano-Structured ZnO" Mater. Res. Soc. Symp. Proc. Vol. 1108 (2008).

REFERENCES

1. A. Janotti, C. G. Van de Walle, "Fundamentals of zinc oxide as a semiconductor", Rep. Prog.Phys. 72, 126501 (2009).

2. F. Oba, S. R. Nishitani, S. Isotani, H. Adachi, and I. Tanaka, "Energetics of native defects in ZnO", J. Appl. Phys. 90, 824 (2001).

3. F. G. Chen, Z. Z. Ye, W. Z. Xu, B. H. Zhao, L. P. Zhu, and J. G. Lv, "Fabrication of p-type ZnO thin films via MOCVD method by using phosphorus as dopant source"J. Cryst. Growth 281, 458 (2005).

4. F. X. Xiu, Z. Yang, L. J. Mandalapu, D. T. Zhao, J. L. Liu, and W. P. Beyermann, "High-mobility Sb-doped p-type ZnO by molecular-beam epitaxy", Appl. Phys. Lett. 87, 152101 (2005).

5. T. Aoki, Y. Shimizu, A. Miyake, A. Nakamura, Y. Nakanishi, Y. Hatanaka, "p-Type ZnO Layer Formation by Excimer Laser Doping", Phys. Stattus Solidi B 229, 911 (2002).

6. D.C. Look, D. C. Reynolds, J. W. Hemsky, R. L. Jones and J. R. Sizelove, "Production and annealing of electron irradiation damage in ZnO", Appl. Phys. Lett. 75, 811 (1999).

7. Y. W. Heo, D. P. Norton, L. C. Tien, Y. Kwon, B.S. Kang, F. Ren, S. J. Pearton, J. R. LaRoche, "ZnO nanowire growth and devices" Mater. Sci. Eng. R 47, 1 (2004).

8. S. K. Hazra and S. Basu, "ZnO p-n junctions produced by a new route", Solid-State Electron. 49, 1158 (2005).

9. Y. I. Alivov, E. V. Kalinina, A. E. Cherenkov et al., "Fabrication and characterization of n-ZnO/p-AlGaN heterojunction light-emitting diodes on 6H-SiC substrates", Appl. Phys. Lett. 83, 4719 (2003).

10. A. Osinsky, J. W. Dong, M. Z. Kauser et al., "MgZnO/AlGaN heterostructure light-emitting diodes", Appl. Phys. Lett. 85, 4272 (2004).

11. O. Lopatiuk-Tirpak, W. V. Schoenfeld, L. chernyak, F. X. Xiu, J. L. Liu, S. Jang, F. Ren, S.J. Pearton, A. Osinsky, P. Chow, "Carrier concentration dependence of acceptor activation energy in p-type ZnO", Appl. Phys. Lett. 88, 202110 (2006).

12. O. Lopatiuk-Tirpak, L. Chernyak, F. X. Xiu, J. L. Liu, S. Jang, F. Ren, S. J. Pearton, A. Osinsky and P. Chow, "Studies of Minority Carrier Diffusion Length Increase in p-type ZnO:Sb", Journal of Applied Physics, 100, 086101 (2006).

13. Y. W. Heo, K. Ip, S. J. Pearton, and D. P. Norton, "The near band-edge emission and photoconductivity response of phosphorus-doped ZnO thin films grown by pulsed laser deposition", Phys. Status Solidi A 201, 1500 (2004).

14. O. Lopatiuk, L. Chernyak, Y. Feldman, K. Gartsman, "Studies of electron trapping in GaN doped with carbon", Thin Solid Films, 515, 4365-4368 (2006).

15. O. Lopatiuk, A Osinsky, L. Chernyak, "Studies of electron trapping in III-nitride semiconductors", Proceedings of SPIE, 6121: H1-H15 (2006).

16. O. Lopatiuk-Tirpak, L. Chernyak, L.J. Mandalapu, Z. Yang, J.L. Liu, K. Gartsman, Y. Feldman, Z. Dashevsky, "Influence of electron injection on the photoresponse of ZnO homojunction diodes", Appl. Phys. Lett., 89, 142114 (2006).

17. W. Burdett, O. Lopatiuk, L. Chernyak, M. Hermann, M. Stutzmann and M. Eickhoff, "Electron injection-induced effects in Mn-doped GaN", Journal of Applied Physics, 96, 3556 (2004).

18. C. Klingshirn, "ZnO: from basics towards applications", Phys. Stat. Sol. (b) 244, 3027 (2007).

19. S. J. Peartpn, "GaN and Related Materials II", Gordan and Breach Science Publishers, The Netherlands, 93-171, (2000).

20. S. Limpijumnong, S. B. Zhang, S. H. Wei et al., "Doping by large-size-mismatched impurities: The microscopic origin of arsenic- or antimony-doped p-type zinc oxide", Phys. Rev. Lett. 92, 155504 (2004).

21. D. C. Look and B. Claftin, "P-type doping and devices based on ZnO", Phys. Stat. Solidi B-Basic Research 241, 624 (2004).

22. T. M. Barnes, K. Olson, and C. A. Wolden, "On the formation and stability of p-type conductivity in nitrogen-doped zinc oxide", Appl. Phys. Lett. 86, 112112 (2005).

23. F. G. Chen, Z. Z. Ye, W. Z. Xu et al., "Fabrication of p-type ZnO thin films via MOCVD method by using phosphorus as dopant source", J. Cryst. Growth 281, 458 (2005).

24. V. Vaithianathan, B. T. Lee, and S. S. Kim, "Pulsed-laser-deposited p-type ZnO films with phosphorus doping", J. Appl. Phys. 98, 043519 (2005).

25. Y. R. Ryu, S. Zhu, D. C. Look et al., "Synthesis of p-type ZnO films", J. Cryst. Growth 216, 330 (2000).

26. V. Vaithianathan, B. T. Lee, and S. S. Kim, "Preparation of As-doped p-type ZnO films using a Zn3As2/ZnO target with pulsed laser deposition", Appl. Phys. Lett. 86, 062101 (2005).

27. F. X. Xiu, Z. Yang, L. J. Mandalapu et al., "High-mobility Sb-doped p-type ZnO by molecular-beam epitaxy", Appl. Phys. Lett. 87, 152101 (2005).

28. M. Levinshtein, S. Rumyantsev, and M. Shur, "Properties of Advanced Semiconductor materials", John Wiley & Sons, New York, 1-30 (2001).

29. D. J. H. Lambert, M. M. Wong, U. Chowdhury, C. Collins, T. Li, H. K. Kwon, B. S. Shelton, T. G. Zhu, J. C. Campbell, and R. D. Dupuis, "Back illuminated AlGaN solar blind photodetectors", Appl. Phys. Lett, 77, 1900, (2000).

30. P. Boguslawski, E. L. Briggs, and J. Bernholc, "Amphoteric properties of substitutional carbon impurity in GaN and AlN", Appl. Phys. Lett. 69, 233 (1996).

31. A. F. Wright, "Substitutional and interstitial carbon in wurtzite GaN", J. Appl. Phys. 92, 2575 (2002).

32. C. R. Abernathy, J. D. Mackenzie, S. J. Pearton et al., "Ccl4 Doping of Gan Grown by Metalorganic Molecular-Beam Epitaxy", Appl. Phys. Lett. 66, 1969 (1995).

33. D. J. As, U. Kohler, M. Lubbers et al., "p-type doping of cubic GaN by carbon", Phys. Stat. Solidi A-Applied Research 188, 699 (2001).

34. R. Armitage, Q. Yang, H. Feick et al., presented at the Proceedings of the 2002 MRS Spring Meeting, 2002.

35. H. Tang, J. B. Webb, J. A. Bardwell et al., "Properties of carbon-doped GaN", Appl. Phys. Lett. 78, 757 (2001).

36. J. Baur, K. Maier, M. Kunzer et al., "Determination of the Gan/aln Band-Offset Via the (-/0)-Acceptor Level of Iron", Appl. Phys. Lett. 65, 2211 (1994).

37. Y. Shon, Y. H. Kwon, Y. S. Park et al., "Ferromagnetic behavior of p-type GaN epilayer implanted with Fe+ ions", J. Appl. Phys. 95, 761 (2004).

38. J. P. Colinge, C. A. Colinge, "Physics of Semiconductor Devices", Kluwer Academic Publishers, The Netherlands, 51-89 (2003).

39. D. J. Roulston, "An Introduction to the Physics of Semiconductor Devices", Oxford University Press, 35-55 (1999).

40. C. Schwarz, L. Yuging, M. Shathkin, E. Flitsiyan and L. Chernyak, "Cathodoluminescence studies of Electron Irradiation Effects in n-type ZnO" J. Phys.: Condens. Matter 23 334204 (2011).

41. C. Schwarz, E. Flitsiyan, L. Chernyak, V. Casian, R. Schneck, Z. Dashevsky, S. Chu, J.L. Liu, "Impact of forward bias injection on minority carrier transport in p-type ZnO nanowires" Appl. Phys. Lett. 110. 056108 (2011).

42. L. Chernyak, C. Schwarz, E.S. Flitsiyan, S. chu, J.L. Liu, K. Gartsman, "Electron beam induced current profiling of ZnO p-n homojunctions". Appl. Phys. Lett 92. 102106 (2008).

43. E.S. Flitsiyan, C. Schwarz, L. Chernyak, R.e. Peale, Z. Dashevsky, W.G. Vernetson, "Neutron Irradiation-Induced Enhancement of Electronic Carrier Transport in ZnO" "Radiation Effects & Defects in Solids" Vol.166, No.2, 104-108 (2010).

44. E.S. Flitsiyan, C. Schwarz, R.e. Peale, O. Lupan, L. Chernyak, L. Chow, W.G. Vernetson, Z. Dashevsky, "Neutron Transmutation Doping and Radiation Hardness for Solution-Grown Bulk and Nano-Structured ZnO" Mater. Res. Soc. Symp. Proc. Vol. 1108 (2008).

45. F. Rinaldi, "Basics of Molecular Beam Epitaxy", Annual report on optoelectronics, 36, 443-462 (2002).

46. P. C. Phua and V. K. S. Ong, "Determining the Location of Localized Defect in the Perpendicular Junction Configuration with the Use of Electron Beam Induced Current," IEEE Trans. Electron. Devices, Vol. 49, Issue 11, pp. 2036 – 2046 (2002).

47. V. K. S. Ong, J. C. H. Phang and D. S. H. Chan, "A Direct Method for the Extraction of Diffusion Length and Surface Recombination Velocity from an EBIC Line Scan: Plane Junction Configuration," IEEE Trans. Electron. Devices, vol. 42, no. 5, pp. 963-968 (1995).

48. J. Boersma, J. J. E. Iindenkleef, and H. K. Kuiken, "A Diffusion Problem in Semiconductor Technology", J. Eng. Math. 18, 315 (1984).

49.   D. S. H. Chan, V. K. S. Ong, and J. C. H. Phang, "A Direct Method for the Extraction of Diffusion Length and Surface Recombination Velocity from an Ebic Line Scan - Planar Junction Configuration", IEEE Transactions on Electron Devices 42, 963 (1995).

50.   C. M. Parish and P. E. Russell, Scanning Cathodoluminescence Microscopy, in Advances in Imaging and Electron Physics, V.147, ed. P. W. Hawkes, P. 1 (2007).

51.   P. R. Edwards and R. W. Martin, "Cathodoluminescence nano-characterization of semiconductors", Semicond. Sci. Technol. 26 064005 9 (2011).

52.   D. S. Jiang, H. Jung, and K. Ploog, "Temperature-Dependence of Photoluminescence from Gaas Single and Multiple Quantum-Well Heterostructures Grown by Molecular-Beam Epitaxy", J. Appl. Phys. 64, 1371 (1988).

53.   O. Lopatiuk-Tirpak, L. Chernyak, L. J. Mandalapu et al., "Influence of electron injection on the photoresponse of ZnO homojunction diodes", Appl. Phys. Lett. 89 (2006).

54.   W. C. Burdett, O. Lopatiuk, A. Osinsky et al., "The optical signature of electron injection in p-(Al)GaN", Superlatt. and Microstruct. 34, 55 (2004).

55.   O. Lopatiuk, L. Chernyak, A. Osinsky and J. Q. Xie, "Lithium Acceptor as a Deep Electron Trap in ZnO", Applied Physics Letters, 87, 214110 (2005).

56.   O. Lopatiuk-Tirpak, L. Chernyak, Y.L.Wang, F.Ren, S.J.Pearton, K. Gartsman, Y. Feldman, "Cathodoluminescence Studies of Carrier Concentration Dependence for the Electron Irradiation Effects in p-GaN", Applied Physics Letters, 90, 172111 (2007).

57.   O. Lopatiuk, A. Osinsky, A. Dabiran, K. Gartsman, I. Feldman and L. Chernyak, "Electron Trapping Effects in C- and Fe-doped GaN and AlGaN", Solid State Electronics, 49, 1662-1668 (2005).

58.   O. Lopatiuk, L. Chernyak, A. Osinsky, J. Q. Xie and P. P. Chow, "Electron-Beam-Induced Current and cathodoluminescence Studies of Thermally Activated Increase for Carrier Diffusion Length and Lifetime in n-type ZnO", Applied Physics Letters, 87, 162103 (2005).

59.   O. Lopatiuk, W. Burdett, L. Chernyak, K. P. Ip, Y. W. Heo, D.P. Norton, S. J. Pearton, B. Hertog, P. P. Chow and A. Osinsky, "Minority carrier transport in p-

type Zn0.9Mg0.1O doped with phosphorus", Applied Physics Letters, 86, 012105 (2005).

60. M. Eckstein and H. U. Habermeier, "Numerical-Analysis of the Temperature-Dependence of Ebic and Cl Contrasts", Journal De Physique IV 1, 23 (1991).

61. Y. Lin, M. Shatkin, E. Flitsiyan, L. Chernyak, Z. Dashevsky, S. Chu, and J. L. Liu, "Minority carrier transport in p-ZnO nanowires" J. Appl. Phys. 109, 016107 (2011).

62. J. I. Pankove, "Optical Processes in Semiconductors", Prentice-Hall, Englewood Cliffs, New Jersey, (1971).

63. R. A. Catlow, S. A. French, A. A> Sokol, A. A. Al-Sunaidi and S. M. Woodley, "Points defects in ZnO", J. Comput. Chem. 29, 2234-49 (2008).

64. W. E. Vehse, W. A. Sibley, F. J. Keller, Y. Chen, "Radiation damage in ZnO single crystals", Phys. Rev. 167, 828-836, (1968).

65. D. C. Look, B. B. Clarflin, "P-type doping and devices on ZnO", Phys. Stat. Sol. (b) 241, 624-631 (2004).

66. W. L. Schaich, "Derivation of single-scattering fomulas for x-ray absortion and high energy electron-loss spectroscopies", Phys. Rev. B 29, 6513-6519 (1984).

67. R. T. Cox, D. Block, A. Herve, R. Picard, C. Santier, R. Helbig, "Defect studies in electron-irradiated ZnO and GaN", Solid State Commun., 25 (2), 77 (1978).

68. N. O. Korsunska, L. V. Borkovska, B. M. Bulakh, L. Yu. Khomenkova, V. I. Kushnirenko, I. V. Markevich, "The influence of defect drift in external electric field on green luminescence of ZnO single crystals", J. Lumin, 102-103, 733 (2003).

69. S. C. Binari, K. Ikossi, J. A. Roussos, W. Kruppa et al, "Trapping Effects and Microwave Power Performance in AlGaN/GaN HEMTs", Electron Devices, 48 Issue:3, 465-471, (2001).

70. C. F. Lo, L. Liu, F. Ren, H.-Y. Kim, et al, "Effects of proton irradiation on dc characteristics of InAlN/GaN high electron mobility transistors" J. Vac. Sci. Technol. B 29, 061201 (2011).

71. C. F. Lo, L. Liu, T.S. Kang, H.-Y. Kim, C. Schwarz, E. Flitsiyan, L. Chernyak et al, "Degradation of dc characteristics of InAlN/GaN high electron mobility transistors by 5 MeV proton irradiation" J. Vac. Sci. Technol. B 30, 031202-1 (2012).